A&A 626, A133 (2019)
https://doi.org/10.1051/0004-6361/201834085

Astronomy & Astrophysics

Sparkling nights and very hot days on WASP-18b: the formation of clouds and the emergence of an ionosphere

Ch. Helling[1,2,3], P. Gourbin[2,4], P. Woitke[1,2], and V. Parmentier[5]

[1] Centre for Exoplanet Science, University of St Andrews, St Andrews, UK
e-mail: Christiane.Helling@st-and.ac.uk
[2] SUPA, School of Physics & Astronomy, University of St Andrews, St Andrews, KY16 9SS, UK
[3] SRON Netherlands Institute for Space Research, Sorbonnelaan 2, 3584 CA Utrecht, The Netherlands
[4] Département de Physique, Université Paris-Sud, Université Paris-Saclay, 91405 Orsay, France
[5] Atmospheric, Oceanic & Planetary Physics, Department of Physics, University of Oxford, Oxford OX1 3PU, UK

Received 14 August 2018 / Accepted 24 January 2019

ABSTRACT

Context. WASP-18b is an ultra-hot Jupiter with a temperature difference of up to 2500 K between day and night. Such giant planets begin to emerge as a planetary laboratory for understanding cloud formation and gas chemistry in well-tested parameter regimes in order to better understand planetary mass loss and for linking observed element ratios to planet formation and evolution.
Aims. We aim to understand where clouds form, their interaction with the gas-phase chemistry through depletion and enrichment, the ionisation of the atmospheric gas, and the possible emergence of an ionosphere on ultra-hot Jupiters.
Methods. We used 1D profiles from a 3D atmosphere simulation for WASP-18b as input for kinetic cloud formation and gas-phase chemical equilibrium calculations. We solved our kinetic cloud formation model for these 1D profiles, which sample the atmosphere of WASP-18b at 16 different locations along the equator and in the mid-latitudes. We derived the gas-phase composition consistently.
Results. The dayside of WASP-18b emerges as completely cloud-free as a result of the very high atmospheric temperatures. In contrast, the nightside is covered in geometrically extended and chemically heterogeneous clouds with dispersed particle size distributions. The atmospheric C/O ratio increases to >0.7 and the enrichment of the atmospheric gas with cloud particles is $\rho_{\rm d}/\rho_{\rm gas} > 10^{-3}$. The clouds that form at the limbs appear located farther inside the atmosphere, and they are the least extended. Not all day- to nightside terminator regions form clouds. The gas phase is dominated by H_2, CO, SiO, H_2O, H_2S, CH_4, and SiS. In addition, the dayside has a substantial degree of ionisation that is due to ions such as Na^+, K^+, Ca^+, and Fe^+. Al^+ and Ti^+ are the most abundant of their element classes. We find that WASP-18b, as one example for ultra-hot Jupiters, develops an ionosphere on the dayside.

Key words. astrochemistry – planets and satellites: atmospheres – solid state: refractory – planets and satellites: gaseous planets – infrared: planetary systems

1. Introduction

WASP-18b is a hot ($T_{\rm equ} \approx 2400$ K) Jupiter of 10 $M_{\rm J}$ and 1.1 $R_{\rm J}$ (Hellier et al. 2009; Sheppard et al. 2017) orbiting a inactive late F6-type host star (Fossati et al. 2014) in 0.94 days on an orbit with a low eccentricity ($e = 0.0085$) and in almost perfect alignment with its host star (Triaud et al. 2010). WASP-18b is an ultra-hot Jupiter and one of the hottest close-in gas giants known so far (Parmentier et al. 2018). Its ultra-short period causes very high irradiation from its F-type star and therefore leads to an extreme temperature difference between day- and nightside (Komacek & Showman 2016). Nymeyer et al. (2011) suggested that WASP-18b has an extremely low Bond albedo and a very inefficient day- to nightside energy redistribution, a conclusion supported by Iro & Maxted (2013) and Schwartz & Cowan (2015). The near *Ks*-band secondary eclipse observations in combination with the previously obtained *Spitzer* data suggests that a better thermal mixing is to be expected at higher pressures deeper in the atmospheres (Zhou et al. 2015). Sheppard et al. (2017) found that WASP-18b might have a non-solar C/O ~ 1 based on a radiative transfer retrieval method that includes a selected number of absorbing species (H_2, H_2O, CH_4, NH_3, CO, CO_2, HCN, C_2H_2, CIA of H_2–H_2, and H_2–He; Gandhi & Madhusudhan 2018). H_2O, TiO, and VO were expected in their dayside emission spectroscopy from secondary eclipse observations with the *Hubble* Space Telescope (HST), but none were found. Arcangeli et al. (2018) found that neglecting H^- as an opacity source and the thermal dissociation of H_2O would push their retrieval results to high C/O ratios for the evaluation of secondary eclipse observations with HST WFC3 (1.1 ... 1.7 μm) and combined with *Spitzer* IRAC (3.5, 5.8 and 8.0 μm), both providing dayside emission spectra. By including both effects, the metallicity was constrained to approximately solar and an atmospheric C/O < 0.85. Arcangeli et al. (2018) confirmed the very low day-night energy redistribution found by previous authors and the presence of a thermal inversion on the dayside.

This paper begins a consistent analysis of cloud formation and gas-phase chemistry on ultra-hot Jupiters and analyses WASP-18b by applying numerical simulations. We post-process 1D profiles from a 3D simulation with our kinetic cloud formation model (nucleation, growth/evaporation, gravitational settling, and element conservation), which includes a detailed gas-phase calculation and evaluates the thermal ionisation of the gas phase. We find that WASP-18b forms clouds on the nightside and that thermal ionisation causes the emergence of an ionosphere on the dayside with Mg, Fe, Al, Ca, Na, and K being the most important electron donors in the collision-dominated parts of the atmospheres. Ti^+ is the most abundant Ti-species

on the dayside, not TiO. The enrichment of the atmospheric gas with cloud particles (dust-to-gas ratio, ρ_d/ρ_{gas}) is rather homogeneously of the order of $\geq 10^{-3}$. The C/O ratio has increased to >0.7 in the cloud-forming regions of the WASP-18b atmosphere.

Our approach is outlined in Sect. 2, which includes a summary of the cloud formation model. Section 3 presents our results for the global cloud properties of WASP-18b, and Sect. 4 the global day-night changes in gas-phase chemistry on WASP-18b. Section 5 offers a discussion on element replenishment representations and a comparison of WASP-18b to HD 189733b and HD 209458b. Section 6 concludes the paper.

2. Approach

We applied the two-model approach that we adopted to study the global and the local cloud formation of HD 189733b and HD 209458b in comparison (Helling et al. 2016). We extracted 1D ($T_{gas}(z)$, $p_{gas}(z)$, $v_z(x,y,z)$) profiles ($T_{gas}(z)$ is the local gas temperature [K], $p_{gas}(z)$ is the local gas pressure [bar], and $v_z(x,y,z)$ is the local vertical velocity component [cm s^{-1}]) from 3D hydrodynamic atmosphere simulations across the globe and used these structures as input for our kinetic non-equilibrium cloud-formation code DRIFT (Woitke & Helling 2003, 2004; Helling & Woitke 2006; Helling et al. 2008a). The 3D thermal and wind structure of WASP-18b were calculated using the SPARC/MITgcm (Showman et al. 2009). We refer to the individual papers regarding more details on the 3D simulations and also the cloud formation modelling (see below). SPARC/MITgcm used here did not implement radiative feedback by clouds. This approach has the limitation of not taking into account the potential effect of horizontal winds on the cloud formation. We note that the cloud formation processes are determined by the local thermodynamic properties that are the result of the 3D dynamic atmosphere simulations. Horizontal winds would affect the cloud formation profoundly if the horizontal wind timescale were of the order of the timescales of the microscopic cloud formation processes. Another aspect is the transport of existing cloud particles through horizontal advection, which cannot be considered in the approach that we follow in this paper. Horizontal advection as transport mechanisms for cloud particles will play a role if the frictional coupling between gas and cloud particles is sufficient. A frictional decoupling emerges for large enough cloud particles or for low enough gas densities, as explored in Woitke & Helling (2003). Horizontal transport will only affect our results if the wind blows in the right direction (night → day), and if the advected cloud particles remain thermally stable. Vertical decoupling is included in the approach used here as part of the cloud formation formalism (Sect. 2.1). Woitke & Helling (2003) have further shown that latent heat release is negligible for the condensation of the materials considered if they are forming from a gas with solar element abundances.

2.1. Kinetic formation of cloud particles from oxygen-rich gases

Cloud formation in extrasolar atmospheres requires the formation of seed particles because giant gas planets have no crust like rocky planets. Rocky planets, such as Earth, sweep up cloud condensation nuclei (CCNs) through sand storms, volcano outbreaks, wild fires, and ocean spray. Condensation seeds provide a surface onto which other materials can condense more easily as surface reactions are considerably more efficient than the sum of chemical gas-phase reactions leading to the formation of the seed. The formation of the first surface out of the gas phase proceeds by a number of subsequent chemical reactions that eventually result in small seed particles. Such a chain of chemical reactions can proceed by adding a molecular unit during each reaction step, for instance (e.g. Jeong et al. 2000; Plane 2013). Goumans & Bromley (2012) have shown, for example, that condensation occurs from small gas-phase constituents such as MgO and SiO, which will lead to the formation of larger units such as Mg_2SiO_4 during the condensation process. It is important to realize that large molecules such as Mg_2SiO_4 or $Ca_4Ti_3O_{10}$ do not exist in the gas phase (see Woitke et al. 2018). In this paper, we follow our kinetic cloud formation approach and refer for details on the theoretical background to the references provided below.

Nucleation (seed formation). We applied the concept of homogeneous nucleation to model the formation of TiO_2, SiO, and carbon seed particles (Helling & Fomins 2013; Lee et al. 2015a, 2018). We considered the simultaneous formation of these three different nucleation species in contrast to our previous works. In order to do so, we combined our previous works (Lee et al. (2015a) (for TiO_2 and SiO) and Helling et al. (2017) (for carbon). The effective nucleation rate, $J_* = \sum_i J_{i=\mathrm{TiO2,SiO,C}}$ [cm^{-3} s^{-1}], determines the number of cloud particles, n_d [cm^{-3}], and hence, the total cloud surface (as sum of the surface of the cloud particles).

Bulk growth/evaporation. It is essential that the seed-forming species are also considered as surface growth material as both process (nucleation and growth) compete for the participating elements (here: Ti, Si, O, and C). We considered the formation of 15 bulk materials (TiO_2[s], Mg_2SiO_4[s], $MgSiO_3$[s], MgO[s], SiO[s], SiO_2[s], Fe[s], FeO[s], FeS[s], Fe_2O_3[s], Fe_2SiO_4[s], Al_2O_3[s], $CaTiO_3$[s], $CaSiO_3$[s], and C[s]) that form from 9 elements (Mg, Si, Ti, O, Fe, Al, Ca, S, and C) by 126 surface reactions (Table B.1). We solved moment equations for the cloud particle size distribution function that considers nucleation, growth/evaporation, gravitational settling, and mixing (Woitke & Helling 2003; Helling & Woitke 2006; Helling et al. 2008a; Helling & Fomins 2013). The growth speed is χ [cm s^{-1}], the sign of which is determined by the effective supersaturation ration, S_{eff}. If $S_{eff} < 1$, $\chi < 0$ and the cloud particles evaporate. The approach presented in Woitke & Helling (2003) that we also use here applies force balance between friction and gravity to derive a size-dependent drift velocity, which is required to determine a drift-dependent growth term in the moment equations (gravitational settling).

In addition to the local element abundances, $\varepsilon(z)$, the local thermodynamic properties $T_{gas}(z)$ and $\rho_{gas}(z)$ (local gas density, g cm^{-3}) also determine if atmospheric clouds can form, to which sizes, ($\langle a \rangle$ [μm] – mean cloud particle size) the cloud particles grow and of which materials s (e.g. TiO_2[s], Mg_2SiO_4[s], $MgSiO_3$[s]) they will be composed. The gravitational settling velocity, v_{drift} [cm s^{-1}], is determined by the local gas density, $\rho_{gas}(z)$, and by the cloud particle size.

Element conservation. An additional set of equations for all involved elements was solved with source and sink terms for nucleation, surface growth and evaporation, and gravitational settling.

Element replenishment. Cloud particle formation depletes the local gas phase, and gravitational settling causes these elements to be deposited for example in the inner

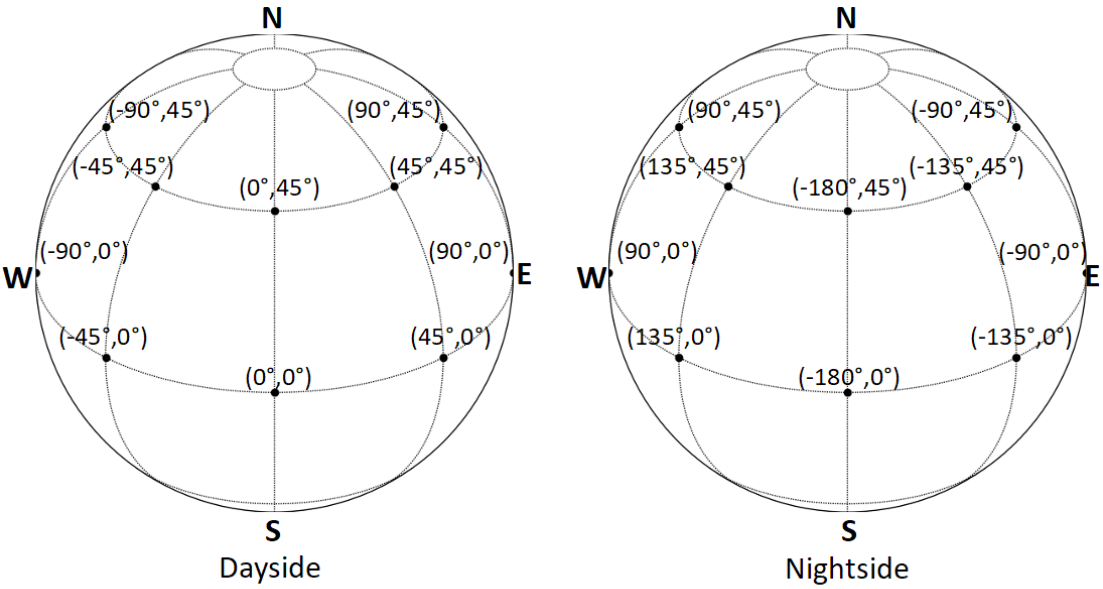

Fig. 1. 3D visualisation of the location of the 16 1D profiles (black dots) that are used to sample the 3D atmosphere for cloud formation, gas-phase chemistry, and thermal ionisation on WASP-18b on the day- (*left*) and the nightside (*right*). The sampled longitudes are $\phi = 0°, 45°, 90°, 135°, -180°, -135°$, and $-90°$, the latitudes are at the equator and $\theta = 0°, 45°$ in the northern hemisphere. The 3D simulations assume that the southern hemisphere is similar to the northern hemisphere. The substellar point is $(\theta, \phi) = (0°, 0°)$, the terminators are at $\phi = 90°, -90°$. The sketches indicate east and west, which need to be quoted with respect to the day- or the nightside, however.

(low-pressure) atmosphere where the cloud particles evaporate. For a stationary cloud to form, element replenishment needs to be modelled. We applied the approach outline in Lee et al. (2015b) (Sect. 2.4) using the local vertical velocity to calculate a mixing timescale, $\tau_{\rm mix} \sim v_{\rm z}(r)^{-1}$. We discuss the use of a constant vertical diffusion coefficient, $\tau_{\rm mix} \sim K_{\rm zz}^{-1}$ in Sect. 5.1.

2.2. Chemical gas composition

We applied chemical equilibrium (thermochemical equilibrium) to calculate the chemical gas composition (represented in terms of number densities $n_{\rm x}$ cm^{-3}) of the atmospheres as part of our cloud formation approach. We used the 1D ($T_{\rm gas}(z)$, $p_{\rm gas}(z)$) profiles and element abundances $\varepsilon_{\rm i}(z)$ (i = O, Ca, S, Al, Fe, Si, Mg, Ti, and C) depleted by the cloud formation processes. All other elements were assumed to be of solar abundance. We used the GGCHEM routines that recently were made publicly available through Woitke et al. (2018). A combination of 156 gas-phase molecules, 16 atoms, and various ionic species were used under the assumption of LTE. The respective material data are benchmarked (Woitke et al. 2018). High velocities and/or strong radiation may cause departure from LTE. Visscher et al. (2006, 2010); Zahnle et al. (2009); Line et al. (2010); Kopparapu et al. (2012); Moses et al. (2011); Venot et al. (2012) have shown that in warm exoplanet atmospheres ($T > 1200$ K), the chemical timescales are in fact short, and thermo-chemical equilibrium therefore prevails in particular in the cloud-forming regions that we are interested in.

No condensates are part of our chemical equilibrium calculations, in contrast to equilibrium condensation models. The influence of cloud formation on the gas-phase composition results from the reduced or enriched element abundances that are due to cloud formation and the cloud opacity impact on the radiation field, and hence, on the local gas temperature and gas pressure. The element depletion or enrichment due to cloud formation is therefore directly coupled with the gas-phase chemistry calculation.

2.3. Input and boundary conditions

Element abundances. We assumed that WASP-18b has an oxygen-rich atmosphere of approximately solar element composition. We used the solar element abundances from Grevesse et al. (2007) (Table A.1) as initial values for the cloud formation simulation and outside the cloud forming domains.

Input profiles from a 3D atmosphere simulation for WASP-18b. We used 1D profiles from a 3D atmosphere code. These were globally distributed as shown in Fig. 1. The geometry is north-south symmetric. The 3D thermal and wind structures were calculated using the SPARC/MITgcm (Showman et al. 2009). The hydrodynamic model solves the primitive equations on a cube sphere grid. It has been successfully applied to a wide range of hot Jupiters (Showman et al. 2009; Parmentier et al. 2013; Kataria et al. 2015, 2016; Lewis et al. 2017), including a few ultra-hot Jupiters (Zhang & Showman 2018; Kreidberg et al. 2018).

Molecular and atomic abundances in the 3D code were calculated using a modified version of the NASA CEA Gibbs minimisation code as part of a previously tabulated grid and were used to explore gas and condensate equilibrium chemistry in substellar objects (Moses et al. 2013; Skemer et al. 2016; Kataria et al. 2015; Wakeford et al. 2017; Burningham et al. 2017; Marley et al. 2017) over a wide range of atmospheric conditions. We considered ≈500 gas-phase species and condensates containing the elements H, He, C, N, O, Ne, Na, Mg, Al, Si, P, S, Cl, Ar, K, Ca, Ti, Cr, Mn, Fe, and Ni. We assumed solar elemental abundances and local chemical equilibrium with rainout of condensate material taken into account, but no interaction between the gas phase and the solid phase.

The opacities of major molecules (CO, H_2O, CH_4, NH_3, TiO, VO, CrH, FeH, CO_2, PH_3, and H_2S), alkali atoms (Na, K, Cs, Rb, and Li), and continuum (collision-induced absorption due to H2–H2, H2–He, and H2–H, bound-free absorption by H and H- and free-free absorption were taken into account following Freedman et al. (2008, 2014). The radiative transfer

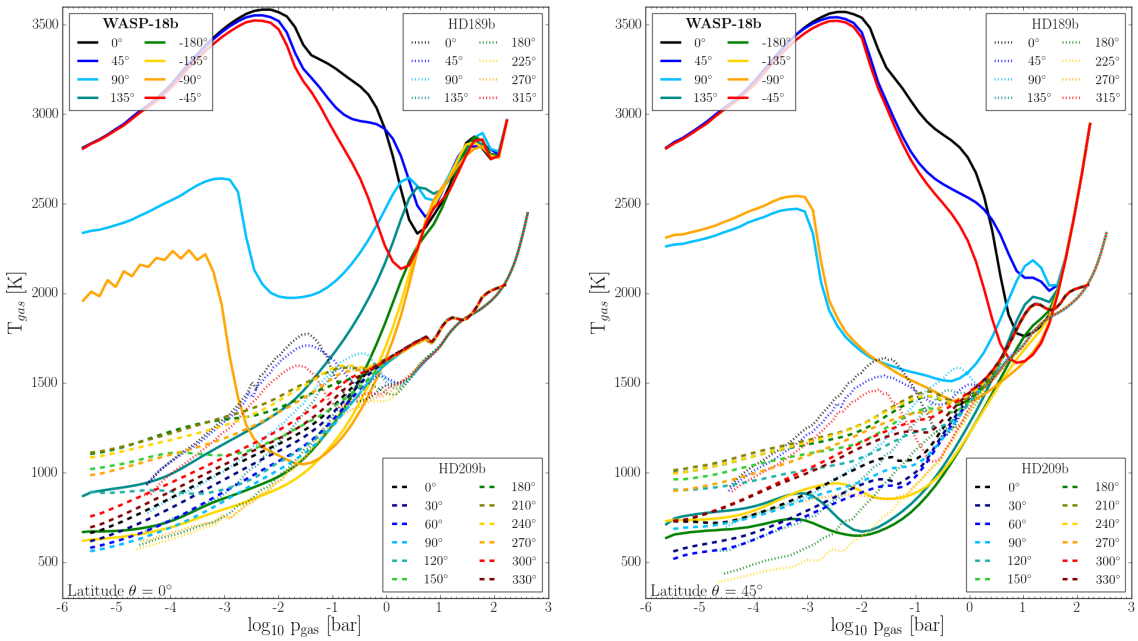

Fig. 2. Input gas temperature, $T_{\rm gas}$ [K], and gas pressure, $p_{\rm gas}$ [bar], for WASP-18b (Arcangeli et al. 2018) in comparison to HD 189733b (Dobbs-Dixon & Agol 2013) and HD 209458b (Mayne et al. 2014). WASP-18b is considerably different from HD 189733b and HD 209458b at the dayside, but similar temperature regimes occur on the nightside.

is performed within 8 k-coefficients inside each of the 11 wavelength bins (Kataria et al. 2015). We used a time step of 25s, ran the simulations for 300 days, and averaged all quantities over the last 100 days. This modelling process is the same as was described in Parmentier et al. (2016), using the WASP-18 system parameters from Southworth et al. (2009).

The model, as all global circulation models studying these hot planets, suffers from some important limitations. The model does not include magnetic interactions between the planetary magnetic field and the ionised gas (Rogers & Showman 2014; Rogers 2017), latent heat transport through the recombination of H_2 (e.g. Bell & Cowan 2018), or cloud opacities (Parmentier et al. 2016; Roman & Rauscher 2017). We therefore expect that large-scale structure such as the day-night contrast or the east-west terminator difference are accurate to within an order of magnitude, but exact temperatures and wind speeds might change (Koll & Komacek 2018, e.g.).

The WASP-18b planetary parameter. We used $T_{\rm equ} = 2411$ K (Sheppard et al. 2017), assumed a constant value $g = 19043$ cm s^{-2} ($R_{\rm P} = 8.328818 \times 10^9$ cm, $M_{\rm P} = 1.979614 \times 10^{31}$ g, Hellier et al. 2009), and a constant mean molecular weight for an H_2-dominated gas ($\mu = 2.3\, m_\mu$). The local gas density $\rho_{\rm gas}(z)$ was calculated from the given gas pressure by applying the ideal gas law, $\rho_{\rm gas}(z) = P_{\rm gas}(z)\mu {\rm m}_\mu / (k_{\rm B} T_{\rm gas}(z))$. In order to determine the height of each of the atmospheric layers inside the 53 vertical computational domains, hydrostatic equilibrium was assumed in vertical direction. The hydrostatic equilibrium equation was integrated to convert the given pressure into a height coordinate. The inner integration boundaries are the planet radius, where $p_{\rm gas} = 1$ bar.

We introduced a small uncertainty by using $\mu = 2.3\, m_\mu$ if H_2 were to dissociate. We show in Fig. A.1 that thermal H_2 dissociation only occurs on the dayside of WASP-18b where no clouds can form. This assumption therefore does not affect our cloud formation results for which the above procedure is required in order to derive the geometric extension of the numerical grid.

3. Global cloud properties of WASP-18b

We study whether clouds might form on WASP-18b, and if they do, what type they are, by sampling eight different profiles at the equator and eight profiles in the mid-latitude region. We endeavoured to provide a first insight into the global and the local cloud structure for a planet that is expected to show vastly different day- and nightsides.

Figure 2 summarises the input profiles that we used to study cloud formation at the day- (longitude $\phi = 0°$, 45°, −45°) and nightside (longitude $\phi = -180°$, 135°, −135°) of WASP-18b as well as at the day- to nightside terminators (longitude $\phi = 90°$ and $\phi = -90°$). The differences in the thermodynamic structures are very large: day- and nightside temperature have a difference of up to 2500 K. The dayside profiles can be as hot as 3500 K at a relatively low pressure of $p_{\rm gas} = 10^{-3}$ bar. The terminator regions show strong temperature inversions that cause a steep local (inward) drop in temperature of up to 1000 K. These thermodynamic differences suggest that cloud and gas-phase chemistry will differ strongly between the day- and the nightside of the planet. This temperature inversion may cause the appearance of emission features that are due to the emergence of an outward-increasing temperature gradient.

WASP-18b in comparison to HD 189733b and HD 209458b. In reference to our previous studies (Helling et al. 2016), Fig. 2 shows the WASP-18b 1D profiles in comparison to the 1D profiles from HD 189733b and HD 209458b. Sources HD 189733b and HD 209458b both have atmospheres that are filled with clouds on the day- and nightside, although their detailed characteristics differ (e.g. cloud particle size and material composition). WASP-18b has a much hotter inner atmosphere than HD 189733b and HD 209458b at the equator and in the hemispheres, but it reaches comparably low temperatures at the nightside. The dayside is hotter by about 2500 K than HD 189733b and HD 209458b in the equator region. The day- to nightside temperature difference for HD 189733b and

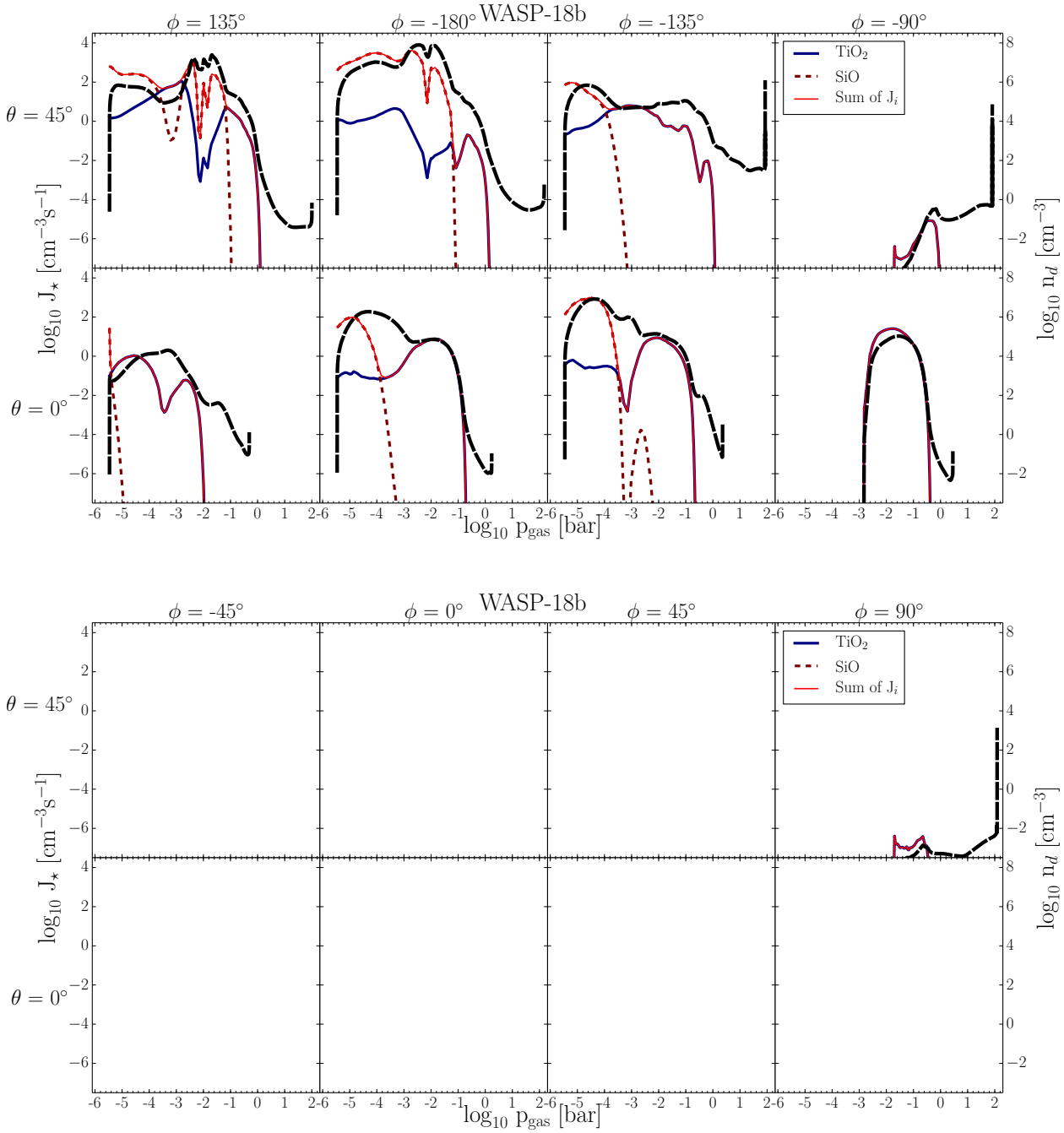

Fig. 3. Seed formation rate, J_* [cm^{-3} s^{-1}], that triggers the cloud formation (left axis) and the resulting cloud particle number densities, $n_{\rm d}$ [cm^{-3}], (right axis, thick dashed line). The total seed formation rate (solid red line) is the sum of the nucleation rate for TiO_2 (solid blue), SiO (dashed brown), and C (dashed grey). Only TiO_2 and SiO form condensation seeds, carbon does not condense in the oxygen-rich environment of WASP-18b. No seed formation occurs on the dayside, therefore no clouds can form, except in the mid-latitudes near the east day- to nightside terminator.

HD 209458b is ≈500 K, compared to the 2000 K on WASP-18b at a local gas pressure of 10^{-5}–10^{-2} bar (see Fig. 2).

Our first result is that no clouds form on the dayside (Fig. 3), therefore a non-depleted warm gas-phase chemistry should be observed. However, a depletion of the gas-phase could occur if cloud particles can be transported horizontally from the nightside to the dayside, and if at the same time, the local supersaturation is high enough to allow for surface growth processes. A depletion of the dayside gas-phase could also occur if the depleted gas from the nightside is faster advected on the dayside than vertical mixing occurs (see Parmentier et al. 2013). In situ cloud formation only takes place in the day- to nightside terminator regions and on the nightside equator and in the hemispheric regions on WASP-18b. The northern dayside terminator profile ($\theta = 45°$, $\phi = 90°$) does form seed particles, but the equator dayside terminator profile ($\theta = 0°$, $\phi = 90°$) remains cloud-free as superrotation affects the equatorial temperature such that the mid-latitudes are colder than the equator (compare also Fig. 2). The supersaturation of the gas is very low ($<10^{-5}$) at the $(\theta, \phi) = (0°, 90°)$ terminator (see Fig. 5). Cloud formation on the dayside therefore remains very unlikely even if condensation seeds were swept along with the winds, given that the

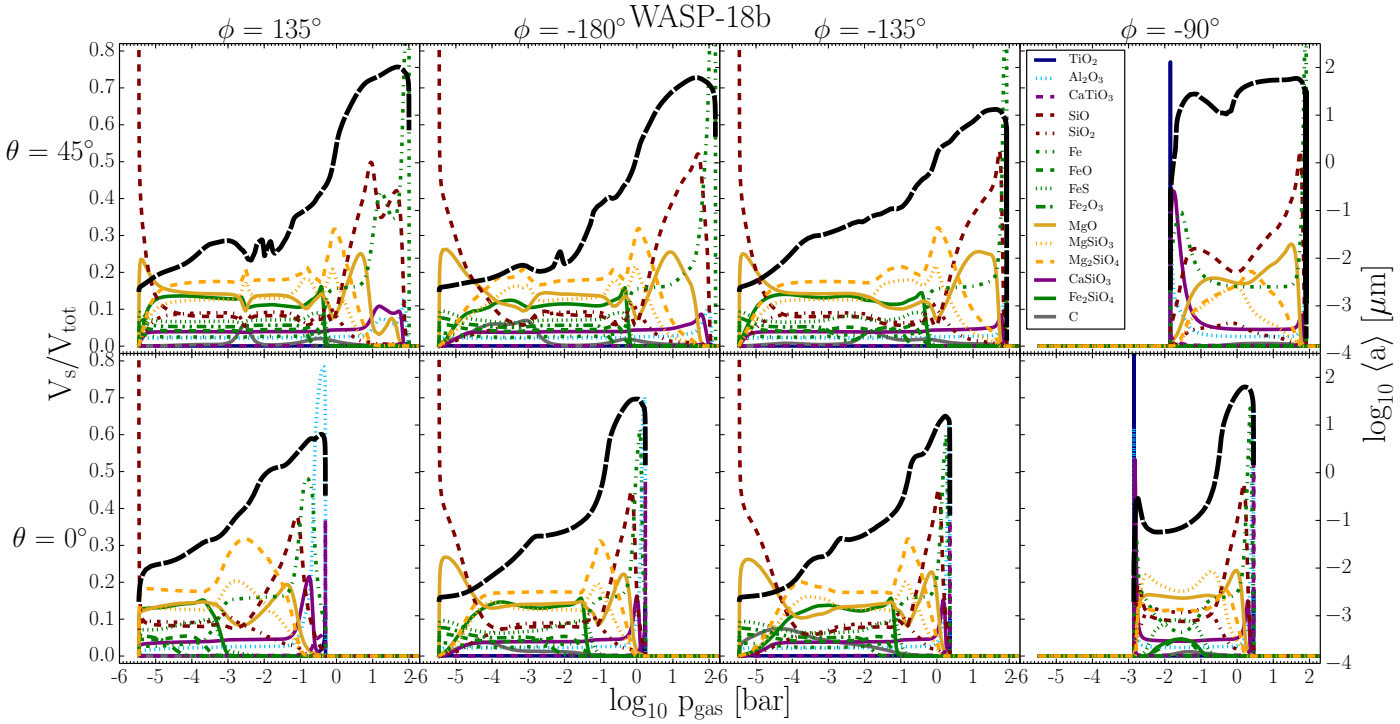

Fig. 4. Cloud structure in terms of material composition (V_s/V_{tot}, $s-15$ solid species, left axis, colour-coded) and the mean cloud particle size ($\langle a\rangle$ [μm], right axis, black dashed) on the nightside of WASP-18b. No clouds form on the dayside of WASP-18b (*top*: 45° north, *bottom*: equator). Some materials reach 100% at the top (SiO[s] (brown dashed), TiO_2[s] (blue solid)) or at the bottom (Fe[s] at $\phi = 135°, -185°$) of the cloud. Carbon (grey solid) appears with a volume fraction of ≈5 − 10% at some locations.

temperatures on the dayside are even higher. On the nightside, a vast amount of cloud particles form, leading to a dust-to-gas-ratio of $\geq 10^{-3}$ and an increase in the atmospheric C/O to >0.7. Arcangeli et al. (2018) derived a disc-averaged C/O < 0.85 from their emission spectre, hence for the dayside of WASP-18b. We predict that the dayside C/O ratio is not affected by cloud formation. If this primordial C/O were close to the upper bound of 0.85, then cloud formation could drive the C/O on the nightside. to values large enough to change significantly the atmospheric chemistry and lead to an observable signature (Helling et al. 2014). Molecules such as HCN and CN might be detectable. The increase in C/O to >0.7 (starting from solar values) only occurs on the nightside in our simulation.

3.1. Nightside of WASP-18b

Figure 3 shows where in the atmosphere WASP-18b cloud formation is triggered through the nucleation of condensation seeds. We considered the simultaneous formation of TiO_2 (solid blue), SiO (brown dashed), and C (solid grey) seed particles (left axis). The sum of these seeds then provides the total number of cloud particles locally (long dashed black lines, right axis). The comparison of the total nucleation rate, J_* [$cm^{-3}s^{-1}$], the cloud particle number density, n_d [cm^{-3}], and Fig. 4 reveals that the vertical cloud extension encompasses a larger volume (plotted in terms of pressure) than the nucleation regions would suggest. This difference demonstrates that cloud particles are transported vertically through gravitational settling into the deeper atmosphere.

Figure 3 further shows that SiO and TiO_2 do efficiently nucleate in the uppermost atmospheric regions until ≈2200 K in the model structures used here. Carbon does not nucleate for all probed profiles. TiO_2 remains also efficient at higher temperatures through the combined effect of element consumption by material growth and temperature. TiO_2 is the sole nucleation species for the hotter nightside east-terminator ($\phi = -90°$) at the equator and in the mid-latitudes.

The dayside of WASP-18b has no seed formation except at the dayside west terminator ($\phi = 90°$). This is a clear indication that WASP-18b will not form any clouds in situ at its dayside because the local temperatures are simply too high. This conclusion is further emphasized by our study of the gas-phase composition in Sect. 4 and Fig. A.12, which shows that Ti^+ is the dominating Ti-carrier at the dayside of WASP-18b, and not TiO_2, as is the case for most of the nightside. Small cloud particles can move along with the flow and could therefore be transported form the night- to the dayside. They could therefore serve as condensation seeds in the absence of in situ seed formation. Our investigation of the local gas-phase shows, however, that the dayside of WASP-18b will be too hot to allow for a sufficient supersaturation of the gas phase for condensation to occur.

Figure 4 presents the vertical cloud extension, their detailed material composition in units of relative volumes (V_s/V_{tot}, s are solid species; the colour code lines are on left axis) and the vertical distribution of the mean cloud particles ($\langle a\rangle$ [μm], the black solid line on right axis) for the equator (bottom row) and the 45° latitude on the northern hemisphere. These 1D cloud maps visualize that the clouds extend over a larger pressure range in the (northern) hemisphere than at the equator region. At the (northern) hemisphere nightside profiles ($\phi = 135°, -180°, -135°$), the entire computational domain is filled with cloud particles. The cloud extension becomes more confined the more westward ($\phi = -135° \longrightarrow -180° \longrightarrow 135°$) we probe the atmosphere on

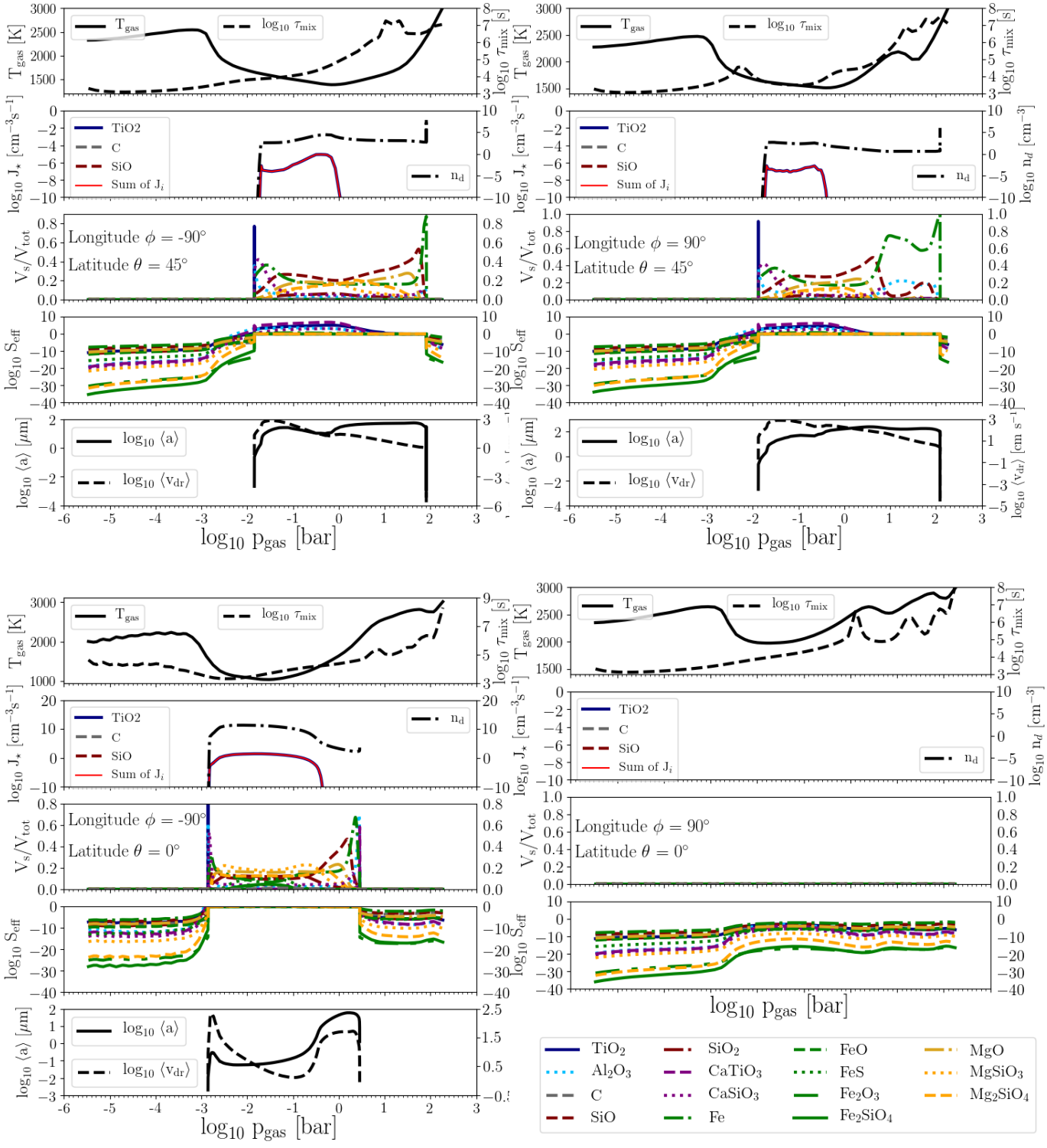

Fig. 5. Combined view of the cloud structure of the profiles probing each of the day- to nightside terminators of WASP-18b (*top*: 45° north, *bottom*: equator; *left*: west, and *right*: east seen from the dayside). Following earlier works (e.g. Fig. 9 in Helling & Casewell 2014), we summarise the fundamental cloud properties for each of the limb profiles to demonstrate the differences in cloud details and their causes. For each profile the plots show the following properties as a function of the local gas pressure p_{gas} [bar]. *First panel*: local gas temperature, T_{gas} [K] (solid, left) and mixing timescale τ_{mix} [s] (dashed, right). *Second panel*: total nucleation rate, J_* [cm^{-3} s^{-1}] (red), and the individual rates for TiO_2 (blue), SiO (brown dashed), and carbon (green dashed); number density of cloud particle, n_d [cm^{-3}]. *Third panel*: effective growth velocity, χ [10^{-7} cm s^{-1}]. *Fourth panel*: material volume fraction, V_s/V_{tot}, with V_s the volume of the material s, and V_{tot} the volume of all cloud particles. *Fifth panel*: effective supersaturation ratio, S_{eff}, per material. *Sixth panel*: mean cloud particle size, $\langle a\rangle$ [μm] (solid, left), and drift velocity v_{drift} [cm s^{-1}]. The materials are line- and colour-coded as follows: TiO_2[s] – solid dark blue line, Al_2O_3[s] – dotted light blue line, C[s] – dashed green line, SiO[s] – dashed brown line, SiO_2[s] – dash-dotted brown, $CaTiO_3$[s] – dashed purple line, $CaSiO_3$[s] – dotted purple line, Fe[s] – dash-dotted green line, FeO[s] – dashed green line, FeS[s] – dotted green line, Fe_2O_3[s] i– long-dash-dotted green line, Fe_2SiO_3[s] – solid green line, MgO[s] – dash-dotted dark orange line, $MgSiO_3$[s] – dotted orange line, Mg_2SiO_4[s] – dashed orange line. Superrotation prohibits cloud formation on the east equatorial terminator ($\phi = 90°$, $\theta = 0°$; lower left panels).

the nightside in the equatorial regions. This confinement does not occur in the northern/southern hemisphere. The mean cloud particle sizes follow the profile of the atmospheric gas, which generally has an outward-decreasing gas density: the cloud particle size increases inwards and reaches its maximum in the densest regions just before it decreases and drops to zero because the local temperature becomes too hot and the cloud particles evaporate. It is interesting to note that the hemispheric ($\theta = 45°, -45°$) day- to nightside terminator at $\phi = -90°$ forms the largest cloud particles as result of a considerably lower nucleation rate.

The material composition of the cloud particles changes as the local thermodynamic conditions change. The topmost layer is determined by the seed-particle-forming materials and MgO[s] for all but the $\phi = -135°$ equator profile. As soon as Mg-Si-O and Fe-Si-O materials become thermally stable, a combination of them makes up the matrix (the bulk) of the cloud particles. Mg_2SiO_4[s], $MgSiO_3$[s], MgO[s], and Fe_2SiO_4[s] make up 60% of the volume, with Mg_2SiO_4[s] and $MgSiO_3$[s] contributing most. This is followed by 20–30% made of SiO[s], SiO_2[s], and FeS[s]. All other materials remain below the 10% level, providing a colourful mix of minerals in the Mg_2SiO_4[s]/$MgSiO_3$[s]-dominated part of the cloud. We note that the cloud particles change in sizes from $\langle a \rangle \approx 10^{-3} \ldots 1$ μm in this cloud region. The temperature increases deeper into the atmospheres at the nightside, which causes the Mg-Si-O/Fe-Si-O materials to become thermally unstable and therefore to evaporate. This results in a substantial material peak of SiO[s] before it evaporates, and the high-temperature condensates determine the material composition of the cloud at its hottest rim at low altitudes. The SiO[s] dominates substantially in the warmer regions. Seventy-five percent of the cloud volume in this layer made of $\approx 1 \ldots 2$ μm sized particles is made of SiO[s] with MgO[s] ($\approx$20%) and Fe[s] ($\approx$15%) with inclusions from $CaSiO_3$[s] and Al_2O_3[s]. The equatorial region again has the smaller particles in this cloud region as well. After SiO[s] has evaporated, a thin cloud layer made of Fe[s] with $CaSiO_3$[s] and Al_2O_3[s] inclusions follows. At the equator, one to two additional cloud regions are made of almost pure Al_2O_3[s], and below this, $CaTiO_3$[s] forms. Al_2O_3[s] and $CaTiO_3$[s] are the most stable materials in our setup. In the mid-latitudes, the largest cloud particles reach sizes of 100 μm and are made of Fe[s] with $CaSiO_3$[s] and Al_2O_3[s] inclusions. In the equator region, the largest particles reach 10 μm and are made of – possibly sparkling – Al_2O_3[s] and $CaTiO_3$[s]. If the cloud particles are heated or are exposed to high pressures, amorphous materials can turn into their crystalline counterparts (e.g. Helling & Rietmeijer 2009), which may cause the clouds to sparkle. The implication of the cloud formation on the gas-phase chemistry is discussed in detail in Sect. 4.

3.2. Day- to nightside terminator clouds on WASP-18b

WASP-18b is interesting with respect to cloud and gas chemistry as its thermodynamic set-up varies greatly over the globe (Sect. 2.3). The change-over between "no clouds" and "many clouds" occurs at the day- to nightside terminators, which we discuss separately here. Both terminator-regions at the equator and in the northern hemisphere show strong temperature inversions that cause an extended local minimum of the temperature inside the atmosphere.

Figure 5 summarizes the cloud details for the four 1D terminator profiles investigated in this paper (top: 45° north, bottom: equator; left: west, and right: east seen from the dayside). The top panel of this figure also shows the input properties ($T_{\rm gas}$, $p_{\rm gas}$) (solid line, left axis) and the mixing timescale, $\tau_{\rm mix}$ (dashed line, right axis). Cloud formation takes place at three out of the four terminators. The east terminator (seen from the dayside; $\phi = 90°$) at the equator is too hot for clouds to form, but winds will not transport cloud particles from the nightside here because the wind moves from the day- to the nightside at $\phi = 90°$. The terminator exposed to the wind from the nightside ($\phi = -90°$) is cold enough for in situ cloud formation.

The vertical cloud extension varies between the equatorial ($p_{\rm gas} \approx 10^{-3}-10^{0.5}$ bar) and the northern and southern hemisphere ($p_{\rm gas} \approx 10^{-2}-10^{2}$ bar) terminator as result of the local temperature. This will have implications for transit spectroscopy. The mean cloud particle sizes vary widely at the equator and less so in the northern and southern hemisphere terminator. Differences also emerge for the material compositions. The northern and southern hemisphere terminators (east and west) have cloud particles that are mainly composed of SiO[s], Fe[s], and MgO[s] and are less strongly dominated by Mg_2SiO_4[s]/$MgSiO_3$[s] with inclusions from other materials. The top and bottom parts of the terminator clouds are dominated by high-temperature condensates: the top is made of thin layers of pure TiO_2[s], followed by a thin layer of a Al_2O_2[s]/$CaTiO_3$[s] mix, and then a thin Fe[s]/$CaTiO_3$[s]-dominated layer with inclusions from Al_2O_2[s], SiO[s] and others to a lesser extent. The bottom layer is made of large Fe[s]-dominated particles with some Al_2O_2[s]. The $\phi = 90°$ terminator region has a substantial Fe[s]-dominated low-altitude layer, in contrast to the $\phi = -90°$ terminator, which has a rather thin Fe[s]-dominated inner layer at low altitudes. The whole low-altitude portion for $p < 1$ bar is made of large particles of $\approx$32 μm that are decelerated by the inward-increasing gas density (dashed line, right axis).

The equatorial terminator that forms clouds on WASP-18b is in the west terminator, seen from the dayside ($\phi = -90°$). Its cloud top is made of subsequent thin layers of TiO_2[s], Al_2O_2[s], $CaTiO_3$[s], and Fe[s]-dominated and becomes more and more a mix of many materials. The main vertical portion of the cloud is made of Mg_2SiO_4[s]/$MgSiO_3$[s]/MgO[s]/SiO[s]/Fe[s] with inclusions from the other materials. The bottom of the cloud changes from SiO[s]-dominated to Fe[s], then Al_2O_2[s], and then $CaTiO_3$[s]-dominated. These bottom cloud layers are composed of the largest particles of $\approx$60 μm that fall with a speed of 1.5 cm s^{-1} (dashed line, right axis).

3.3. Cloud particle load of the atmosphere of WASP-18b

An interesting measure regarding the cloud particle load of the atmosphere is the so-called dust-to-gas mass ratio, $\rho_{\rm dust}/\rho_{\rm gas}$ (Fig. 6, top). This measure for the enrichment of a gaseous medium with condensates (often solid) is widely used in disc modelling where it is set to a constant value (e.g. Alessi & Pudritz 2018), or to study the dust enrichment of cometary tails (e.g. Fulle et al. 2010; Langland-Shula & Smith 2011) or AGB star envelopes (e.g. Helling et al. 2000; Ramstedt et al. 2011). Woitke et al. (2018) have demonstrated that the dust-to-gas mass ratio changes with temperature for a system in thermal equilibrium (i.e. everything that can condense has condensed). The main contributors are materials involving Al, Ca, Fe, Si, and Mg. Condensates composed of titanium, nickel, vanadium, chromium, manganese, sodium, and potassium contribute only very little as their initial element abundances are very low. The maximum value reached in thermal equilibrium is $\rho_{\rm dust}/\rho_{\rm gas} \approx 0.004-0.0052$ for gases >500 K and (Fig. 5 in Woitke et al. 2018).

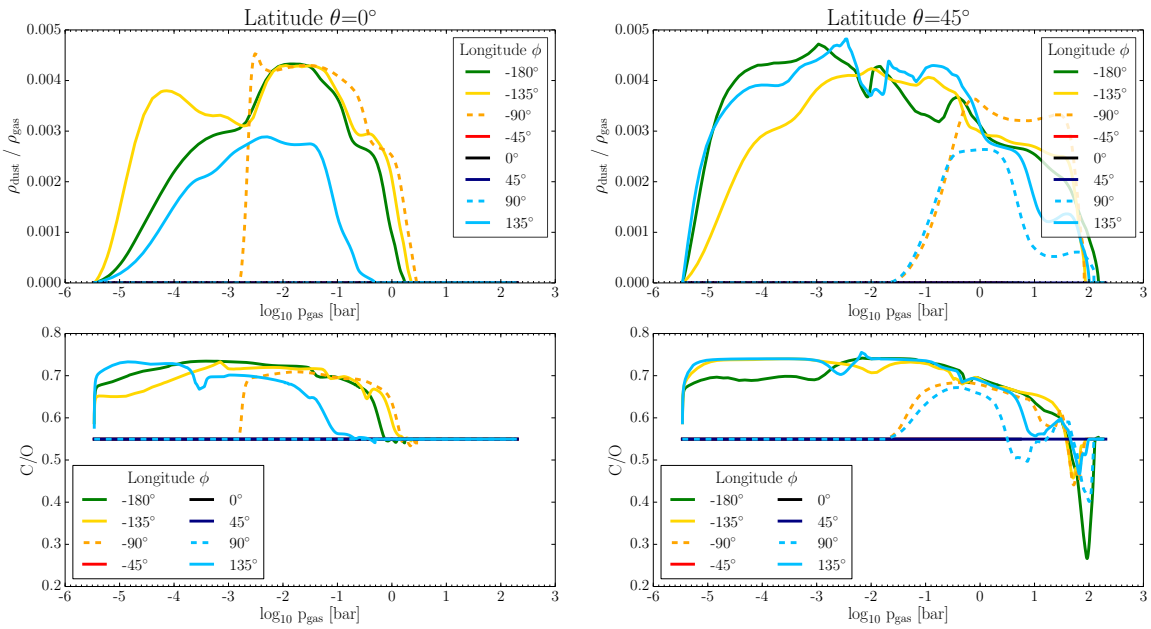

Fig. 6. Cloud particle load in terms of mass density ratios (*top*; $\rho_{\rm dust}/\rho_{\rm gas}$) and the C/O element ratio (*bottom*) at the equator (*left*) and in the northern hemisphere (*right*) of the WASP-18b atmosphere profiles. C/O remains at the solar value of 0.53 for profiles without forming clouds ($\phi = -45°, 135°$). For other mineral ratios such as Fe/Si and Mg/Si, we refer to Appendix A (Figs. A.2 – A.12).

The cloud particle load of the atmospheric gas in WASP-18b varies vertically with the maximum of $\rho_{\rm dust}/\rho_{\rm gas} \approx 0.0042$ being reached at $p \approx 10^{-2}$ bar in the equatorial region and $\rho_{\rm dust}/\rho_{\rm gas} \approx 0.0049$ at a lower pressure of $p \approx 10^{-3}$ bar in the mid-latitudes on the nightside. $\rho_{\rm dust}/\rho_{\rm gas}$ clearly shows that the cloud layers are located much farther inside the atmosphere and are considerably less extended at the day- to nightside terminators. This indicates the transitional character of the planet's limbs, where a hot dayside transits into a cold nightside. No one $\rho_{\rm dust}/\rho_{\rm gas}$ can describe the profiles studied here. However, the $\rho_{\rm dust}/\rho_{\rm gas}$ is of the order of 10^{-3} for all probed profiles, suggesting a globally rather homogeneous cloud particle load in regions where clouds form.

4. Global changes of the atmospheric gas composition on WASP-18b

The large temperature (and pressure) difference between the day- and nightside on WASP-18b and the transitional character of the terminator regions lead to a distinct cloud distribution on WASP-18b. We therefore expect the atmospheric gas composition on WASP-18b to be vastly different on the day- and nightside as well. We have considered 15 materials that affect the element abundances of the nine elements (Mg, Si, Ti, O, Fe, Al, Ca, S, and C) by cloud particle growth and evaporation by 126 surface reactions. The growth process reduces the element abundances, and the evaporation process enriches the element abundances. The nucleation process has only very little affect on the element involved (Si, Ti, O, and C), but it is strongly affected by element depletion.

4.1. Element depletion and enrichment

One of the most important outcomes of a cloud formation model is the feedback on the gas phase through element depletion or enrichment. The essential quantities to start with are the element abundances because the number of elements needs to be conserved for each element individually. Figure 7 shows the consistency of our cloud formation model because cloud formation only affects the involved elements at the nightside and at the day- to nightside terminators.

Each of the elements is individually depleted, and the depletion varies widely through the cloud structure (along the pressure axis) and across the globe. The largest variations in element depletion for any one element occur along the equator for WASP-18b (Fig. 7, left plots). The day- to nightside terminators stand out by depleting a less extended atmosphere of the vertical atmosphere at the equator and in the hemispheres.

A closer look at Fig. 7 shows that the individual depletion of the elements varies by order of magnitudes. Ti is most strongly depleted, but it also has the smallest initial element abundance of all involved cloud-forming elements. Some elements show a substantial enrichment at the inner cloud boundary located at low altitudes, which is due to the evaporation of cloud particles that have been falling until such high temperatures. Most noticeable is the effect in the mid-latitudes (right panel of Fig. 7) for Ti, O, Ca, Al, and Fe. Si is enriched as well compared to the initial solar values, but far less so than the other elements. Therefore, element enrichment occurs in deep, unobservable layers of the atmosphere. Observable layers are expected to be depleted in all elements that are involved in cloud formation.

Oxygen is one of the most abundant elements in a solar set of element abundances, and it is involved in almost every growth material that easily forms. We therefore show the oxygen-depletion also as C/O ratio in Fig. 6.

4.2. C/O and [X/Si] element ratio

The most prominent element ratio studied in the literature is the carbon-to-oxygen ratio, C/O. C/O is of interest with respect to planet formation scenarios and the link to the chemistry in planet-forming disc (e.g. Helling et al. 2014; Eistrup et al. 2018). C/O, Mg/Si, and Fe/Si are discussed in the literature as control parameters for the amount of carbides and silicates formed in

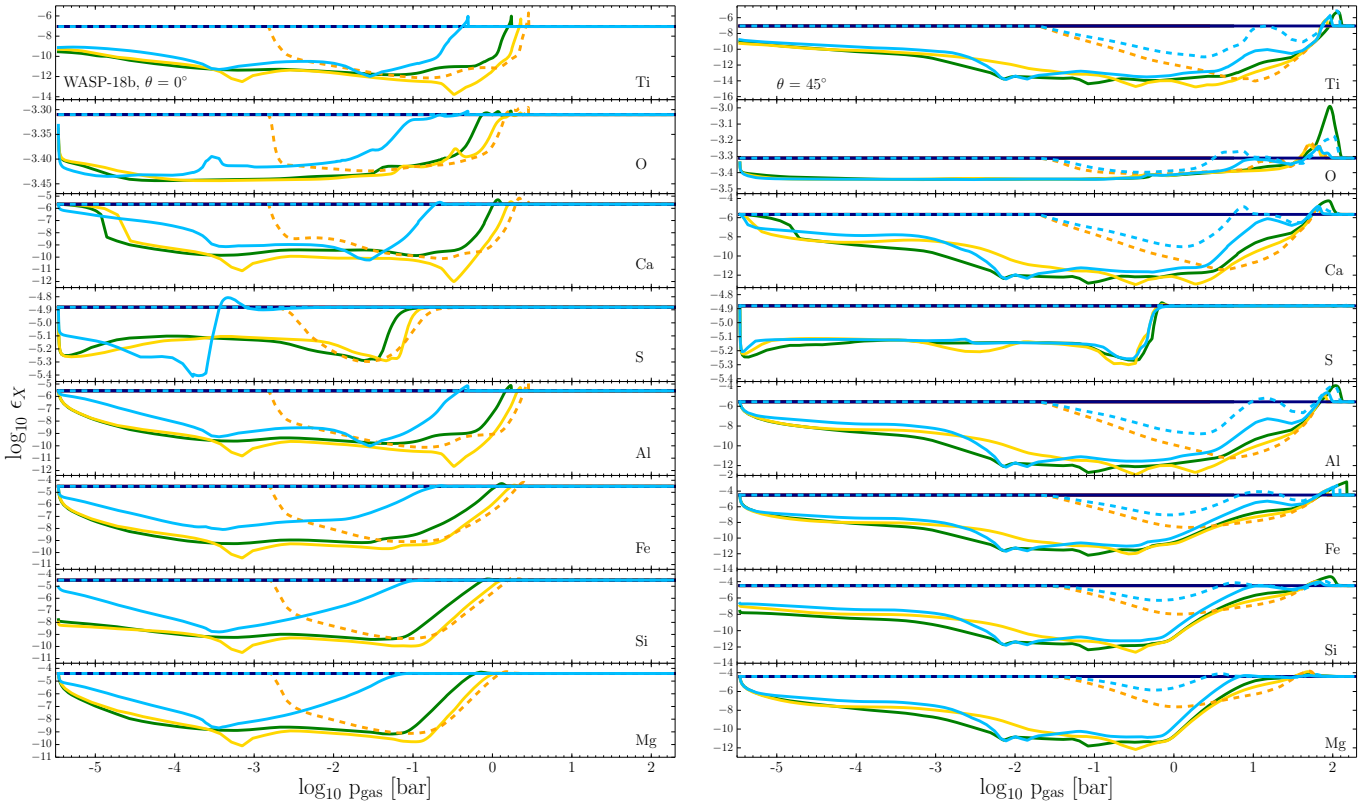

Fig. 7. Abundances, ϵ_x, of the elements that are involved in cloud formation for the equatorial (*left*, $\theta = 0°$) and the northern hemisphere (*right*, $\theta = 45°$) profiles of WASP-18b. The colour code for the atmospheric profiles is the same as in Fig. 6 and all figures throughout the paper. The day-to nightside terminators are depicted as dashed lines. Straight lines indicate no element depletion for these longitudes. Cloud formation mostly causes element depletion. Element enrichment occurs where cloud particles evaporate, most noticeable for ϵ_O. The element abundances change due to cloud formation throughout the atmosphere and across the globe. The clouds affect the element abundances over a larger pressure range at the northern (southern) hemisphere than at the equatorial region.

planets (Adibekyan et al. 2017; Suárez-Andrés et al. 2018). Our results show that the thermodynamic properties of the local gas determine the condensation processes from which element ratios such as C/O (Fig. 6) and X/Si (Figs. A.2 – A.12) result.

The largest change in the C/O throughout the cloud-affected part of the atmosphere occurs in the northern/southern hemisphere. Here the highest and lowest C/O is reached. C/O is bound between 0.28 and 0.73. Only a C/O ration above 0.93 will allow first carbon-binding molecules to emerge (TiC; Woitke et al. 2018). Bedell et al. (2018) showed that C/O varies between 0.4 and 0.6 for the solar twins in the solar neighborhood. No one atmospheric C/O will suffice to describe the atmosphere of WASP-18b. First, it varies vertically throughout the atmosphere, and it varies globally. C/O remains solar at the dayside where no clouds form and becomes enriched/depleted on the cloud-forming nightside. The C/O at the nightside changes from a thermally stable to a thermally unstable cloud. C/O increases above the initial (solar) value of 0.53 in the thermally stable part of the atmosphere, but decreases substantially where the cloud particles evaporate. The increase in C/O is mainly caused by oxygen consumption, and the decrease in C/O is mainly caused by oxygen being transported into deeper atmospheric regions as a result of falling cloud particles. The width of the O-enriched zone shows that the cloud particles do not evaporate instantaneously. If carbon materials form, carbon depletion or enrichment will affect the C/O ratio as well. Our calculations show the condensation of only very little carbon on the nightside of WASP-18b (5–10%; Fig 4).

Similar behaviour occurs for all elements involved in the cloud formation processes, and the detailed results for [X/Si] are provided in Appendix A, where each figure shows the gas-abundance and the respective X/Si curve (thick black dashed line). Bedell et al. (2018) showed that their Mg/Si for solar twins in the solar neighbourhood is greater than one. Our initial undepleted $(Mg/Si)^0 = 1.23$[1] and cloud formation pushes Mg/Si as high as 8 at the inner cloud boundary at the $\phi = -90°$ terminator (Fig. A.8), and well above 4 at the inner cloud boundary of all other cloud-affected profiles we probed. Mg and Si are tightly correlated in the regions where both participate in cloud formation, but the inner low-altitude cloud regions are more affected by SiO than any Mg-binding condensate. This means that the high Mg/Si occurs where Si is still strongly depleted, which is also reflect in the Si/O (Fig. A.10). Fe/Si shows similar features in regions where Si is strongly depleted, for example, in the nucleation zone at $\phi = -134°$ (Fig. A.6). In principle, this holds true for all the other mineral ratios. Examples such as K/Si and Na/Si demonstrate very well where the Si depletion begins because K and Na are not depleted (Figs. A.7 and A.9) because they do not condense in the temperature regimes of WASP-18b. Consequently, the gas with the lowest metallicity exhibits the highest

[1] Bedell et al. (2018); Bond et al. (2010) cited $(Mg/Si)^0 = 1.05$ based on the element abundance data from Asplund et al. (2005) with $\epsilon^0_{Mg} = 7.53$. We used Asplund et al. (2009) with $\epsilon^0_{Mg} = 7.6$. Both sources used $\epsilon^0_{Si} = 7.51$.

Mg/Si. The detailed finding for the mineral ratios are provided in Appendix A.

Woitke et al. (2018) investigated the change of the gas-phase C/O ratio in the limiting case of thermal stability, which allows considering the effect of complex materials such as phyllosilicates. Their results demonstrate that the condensation of Mg/Si/O-binding minerals increases C/O to >0.7, and that a further increase to >0.8 is caused when phylosilicates are included. They also reported that deriving the C/O ratio from a gas solely consisting of H/C/N/O as elements leads to false results compared to the whole set of solar elements.

The changing element ratios demonstrate that an atmospheric ratio (e.g. for C/O) will differ from the bulk value or in fact from any value derived for the warmer, deeper atmospheric regions. The pristine unaltered atmospheric element ratios should be recovered. An added complication may arise for an extended inner low-altitude cloud that is enriched by elements (C/O decreases) rather than depleted (C/O increases).

4.3. Composition of the neutral gas-phase on WASP-18b

The most direct information about an atmosphere can be derived when gas species can be observed spectroscopically because individual atoms and molecules are fingerprints for specific temperature and pressure regimes. Such a direct access is hampered when clouds form, but WASP-18b provides us with a cloud-free dayside. Figures A.1–A.12 provide a detailed account of the gas-phase composition of the atmosphere of WASP-18b sorted by elements. Each of the plots contains an element ratio (C/O, Si/O, Mg/Si, Na/Si, etc.) that allows us to trace the cloud-forming regions, as discussed in Sect. 4.2. Here, we consider features of general and also of specific interest in order to build our understanding for the chemical composition in such thermodynamically diverse planets.

The most abundant species of the collision-dominated parts of the atmospheric gas on WASP-18b are in decreasing order H_2, CO, SiO, H_2O, SiS, and MgH on the dayside. This hierarchy changes somewhat on the nightside to H_2, CO, H_2O, CH_4, and H_2S. The most abundant gas-phase species are neutral molecules despite the large temperature difference between day and night (Fig. 8). A summary of dominating gas species is provided in Table 1.

Although H_2 is the most abundant molecule, it is not the most abundant H-binding species everywhere. This has recently been pointed out by Arcangeli et al. (2018). The dayside of WASP-18b is dominated by atomic hydrogen, H, up to 10^{-2} bar, and at the day- to nightside terminators up to 10^{-3} bar (Fig. A.1). We note that at the equatorial $\phi = -90°$-terminator, H and H_2 appear with very similar number densities. The nightside is H_2 -dominated as the gas temperature is too low for thermally dissociating H_2.

For the O-complex, CO does dominate the gas phase on the dayside, followed by atomic oxygen in the outer layers and by H_2O in regions of high densities. The nightside is affected by the thermodynamics of the atmosphere and element depletion of oxygen through the formation of silicates. The drop in CO correlates well with the peak in C/O, which indicates efficient cloud formation, and it is compensated for by an increase in CH_4 and H_2O (see $\phi = -135°, -180°$, Fig. A.2).

The elements aluminium and titanium play a key role for cloud formation because they form materials that are thermally stable up to rather high temperatures compared to Mg/Si/Fe/O silicates. The Al and the Ti complex (Figs. A.3 and A.12) both replicate what is commonly observed for alkali metals (Na, K, and Ca): their positive ions become more abundant than the neutral atom than any of their neutral counterparts: the Al-complex (Fig. A.3) is dominated by AlH in the high-altitude atmosphere on the nightside, Al^+/Al at the dayside, and Al/AlOH/AlH at the day- to nightside terminator. The equatorial area at $\phi = -90°$ is dominated by atomic aluminium. The Ti complex (Fig. A.12) is dominated by TiO_2 on the nightside ($\phi = 135°, -180°, -135°$), Ti^+/Ti at the dayside, and Ti/TiO at the limbs ($\phi = 90°, -90°$)

Neither Fe not Si exhibit an ion that is more abundant than any of their neutral atoms or molecules. The C complex is dominated by CO in almost all profiles, except for the northern profiles at the nightside (Fig. A.4).

Figure 8 shows how profoundly the globally changing thermodynamic structure affects the local molecular number densities (day-night difference). The strong effect of cloud formation on the actual values (the overplotted C/O serves as guide for the cloud location on the pressure axis) of atoms and molecules is equally clear.

4.4. Dayside ionosphere of the partially ionised atmosphere of WASP-18b

Brown dwarfs have a long tradition of being studied as analogues for giant gas planets because spectral observations are more feasible than for extrasolar planets (e.g. Charnay et al. 2018). Brown dwarfs irradiated by white dwarfs have recently been discovered, and emission lines that originate from heated upper atmospheric regions at high altitudes have been observed from the irradiated brown dwarf WD0137-349B (Longstaff et al. 2017). While the specific ionised species (Fe^+ vs. Na^+) observed will be determined by the temperature that can be reached in these hot outer regions, WASP-18b has a hot enough dayside for atomic ions to emerge.

Dominating ions. The temperature on the dayside of WASP-18b is high enough for various elements to appear in their second ionisation state (singly ionised), as shown in Fig. 8 (top). The most abundant ions that are also more numerous than the neutral atoms are Na^+, K^+, and Ca^+. Al^+ and Ti^+ are also more abundant than their atomic form (Fig. A.3 and A.12), but are far less numerous than Na^+, K^+, or Ca^+. H^- is far more abundant at the dayside and in the terminator regions than at the nightside, but it never is the dominating H-species. This supports the finding in Arcangeli et al. (2018). The most important electron donors on the dayside of WASP-18b are Mg, Fe, Al, Ca, Na, and then K. Mg and Fe have been identified as dominating electron donors in the inner, warmest low-altitude parts of non-irradiated giant gas planet and brown dwarf atmospheres (Rodríguez-Barrera et al. 2015).

Possible emission. We note that the atomic hydrogen abundance, as well as that of Al^+, Ti^+, and Fe^+ (and atomic O, C, and Si), increases outwards where the local temperature increases outwards on WASP-18b. This may suggest that WASP-18b shows emission from Hα (and O, C, Si, Al^+, Ti^+, and Fe^+) from its dayside and terminator regions. Possible emission lines could include $\lambda = 4243.47, \ldots, 5262.02, \ldots, 7494.75, \ldots, 8286.72$Å for Fe^+ (Fe II), $\lambda = 6231.06, \ldots, 6822.69, \ldots 8925.81$Å for Al^+ (Al II), $\lambda = 8445.44$Å for O (OI) (e.g. as seen in post-AGB stars by Arkhipova et al. 2018), $\lambda = 4571.98, 5129.15$Å for Ti^+ (Ti II), $\lambda = 8824.221$Å for Fe (Fe I) (e.g. as seen in accretion outburst of an M5 dwarf with a proto-planetary disc by Sicilia-Aguilar et al. 2017). The occurrence of these lines will depend on the local temperature and density, and a proper radiative transfers calculation are required to provide a

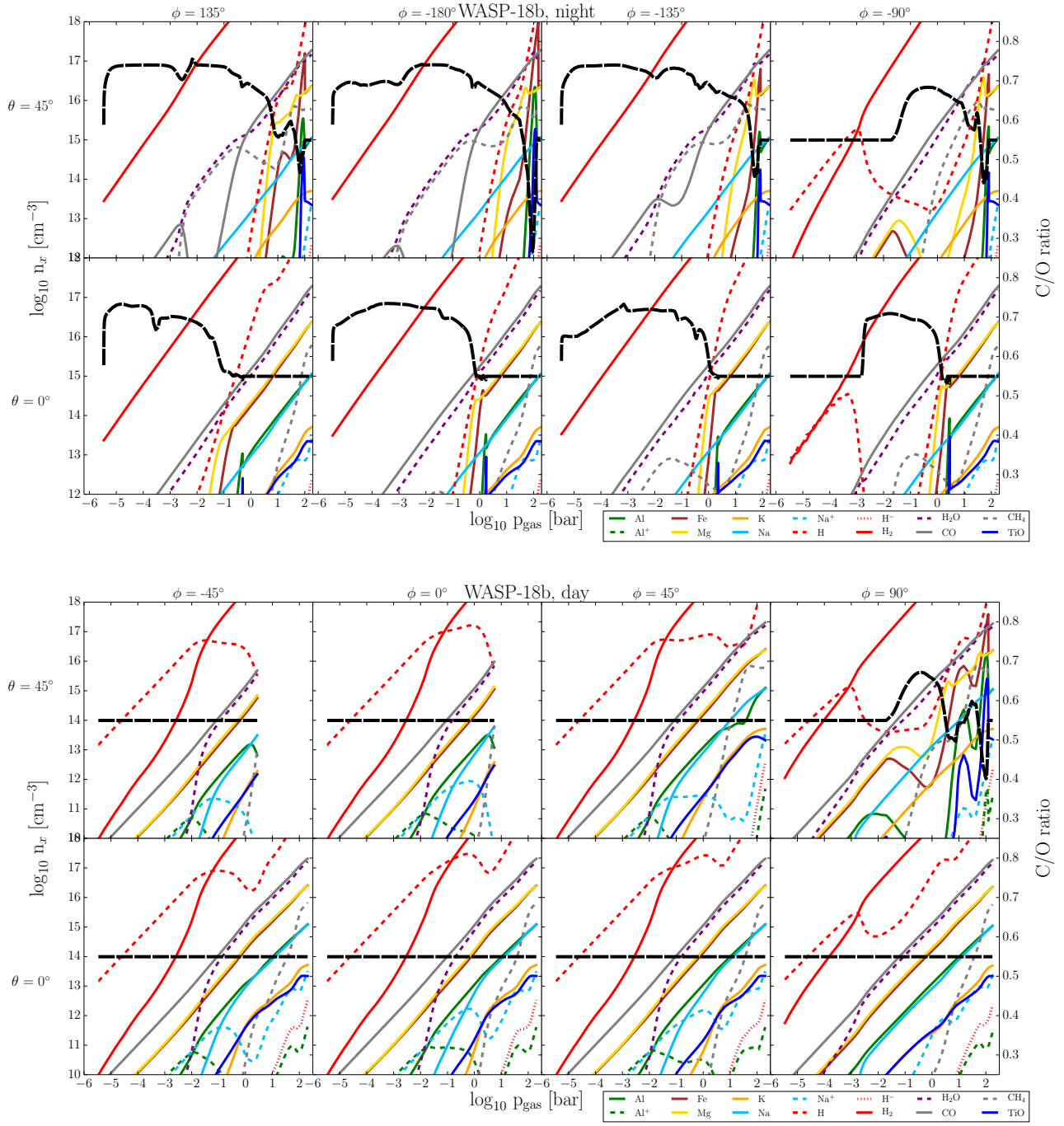

Fig. 8. Composition of the atmospheric gas in chemical equilibrium with respect to the most abundant molecules, atoms, and ions (number density n_x [cm^{-3}]) from the night- (*top*) to the dayside (*bottom*) on WASP-18b. The day- and nightside have very different chemical atmosphere gas compositions. The dayside is dominated by atomic H, the nightside by H_2. The next most abundant gas species are CO, H, or H_2, depending on (θ, ϕ). C/O is over plotted to visualise where clouds form. C/O remains at its initial (solar) value on the dayside where no clouds are forming, but increases on the nightside. A complete account of all species per element is provided in Appendix A.

more profound theoretical support for this suggestion. Hα is used as a measure for planetary mass loss. The possibility of mass loss on ultra-hot Jupiters was discussed in Lothringer et al. (2018) for the hottest example of the super-hot Jupiters, KELT-9b.

Dayside ionosphere on ultra-hot Jupiters. The changing state of thermal ionisation of the individual elements causes a difference of 15 orders of magnitude in the local degree of thermal ionisation, f_e, between the day- and the nightside on WASP-18b (Fig. 9). The nightside is cool enough for only little thermal ionisation to occur in almost the entire vertical atmosphere. The degree of ionisation on the dayside reaches an approximately constant level at $p < 10^{-2.5}$ bar of $f_e \approx 10^{-4.5}$. Most of the high-altitude atmosphere on the dayside and at the day- to nightside terminators has $f_e > 10^{-7}$. The value of $f_e > 10^{-7}$ has been suggested to be a threshold above which a gas may exhibit plasma behaviour without being fully ionised (Rodríguez-Barrera et al. 2015). Hence, the dayside of WASP-18b can be expected to show plasma phenomena, including magnetic field coupling. This conclusion is in line with works

Table 1. Dominating gas-phase species per element for WASP-18b.

	Day	Night	Terminators	
			Longitude $\phi = -90°$	Longitude $\phi = 90°$
Al	$p < 10^{-2}$ bar: Al^+ $p > 10^{-2}$ bar: Al at high p_{gas}: AlH, AlOH	AlOH, AlO_2H at high p_{gas}: Al, Al^+	$p_{gas} < 10^{-2}$ bar: Al $p_{gas} > 10^{-2}$ bar: AlOH at high p_{gas}: Al, AlH, AlOH	Lat $\theta = 45°$: $p_{gas} < 10^{-2}$ bar: Al $p_{gas} > 10^{-2}$ bar: AlOH at high p_{gas}: Al, AlH, AlOH. Lat $\theta = 0°$: $p_{gas} < 10^{-3}$ bar: Al^+ $p_{gas} > 10^{-3}$ bar: AlH, AlOH at high p_{gas}: Al, AlH, AlOH
Ca	$p_{gas} < 10^{-2}$ bar: Ca^+ $p_{gas} > 10^{-2}$ bar: Ca	$p_{gas} < 10^{-3}$ bar: $Ca(OH)_2$, $CaCl_2$ $p_{gas} = 10^{-3}$–< 1 bar: $Ca(OH)_2$ p_{gas} >1bar: Ca	Ca if clouds: $Ca(OH)_2$, $CaCl_2$	Ca
C	CO	CO, CH_4	CO; CH_4 at high p	CO; CH_4 at high p
Fe	Fe, Fe^+	Fe; low p_{gas}: $Fe(OH)_2$ high p_{gas}: FeH	Fe	Fe
H	$p_{gas} < 10^{-1}$ bar: H $p_{gas} > 10^{-1}$ bar: H_2	H_2; at high p_{gas}: H	H_2; $p_{gas} < 10^{-3}$ bar: H	H_2; $p < 10^{-3}$ bar: H
Mg	Mg; $p_{gas} < 10^{-2}$ bar: Mg^+ (many differences for Mg at each profile)	Lat $\theta = 45°$: $p_{gas} < 10^{-3}$ &$p_{gas} > 10^{-1}$: Mg $p_{gas} = 10^{-3}$–10^{-1} bar: $Mg(OH)_2$ Lat $\theta = 0°$: Mg $p_{gas} < 10^{-4}$ bar: $Mg(OH)_2$ highest p_{gas}: MgH	Mg MgH at high p_{gas}	Mg MgH at high p_{gas}
O	CO, $p_{gas} < 10^{-2}$ bar: O $p_{gas} > 10^{-2}$ bar: H_2O	CO, H_2O	CO all p_{gas}/ p_{gas}>10^{-3} bar: H_2O	CO; $p_{gas} > 10^{-3}$: H_2O
Si	$p_{gas} < 10^{-2}$: Si $p_{gas} > 10^{-2}$: SiO	SiS, SiO	SiO	SiO
S	low p_{gas}: S high p_{gas}: H_2S	H_2S	$p_{gas} < 10^{-3}$: S $p_{gas} > 10^{-3}$: H_2S	$p_{gas} < 10^{-3}$: S $p_{gas} > 10^{-3}$: H_2S
Ti	$p_{gas} < 10^{-2}$: Ti^+ $p_{gas} > 10^{-2}$: Ti, TiO	$p_{gas} < 1$ bar: TiO_2 $p_{gas} > 1$ bar: TiO highest p_{gas}: Ti	TiO TiO_2 when clouds form	TiO $p_{gas} < 10^{-3}$/ highest p_{gas}: Ti

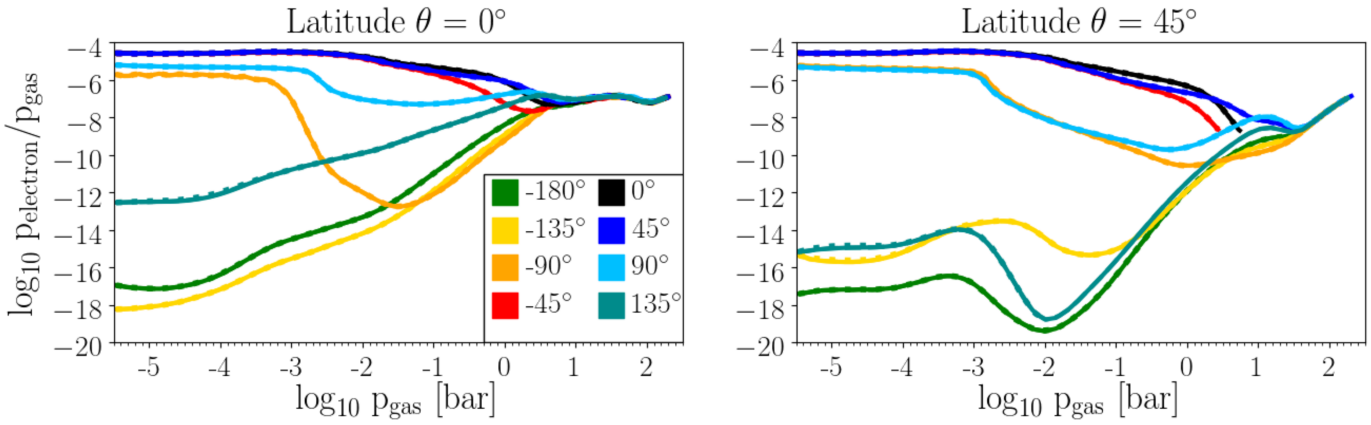

Fig. 9. WASP-18b dayside ionosphere as a result of a partially ionised gas in the atmosphere ($\phi = -90°, -45°, 0°, 45°$, and 90°): the degree of thermal ionisation from the day- to the nightside at the equator (*left*) and in the northern hemisphere (*right*) of WASP-18b. The ionosphere is stronger in the equatorial regions ($\theta = 0°$) than in the northern hemisphere ($\theta = 45°$).

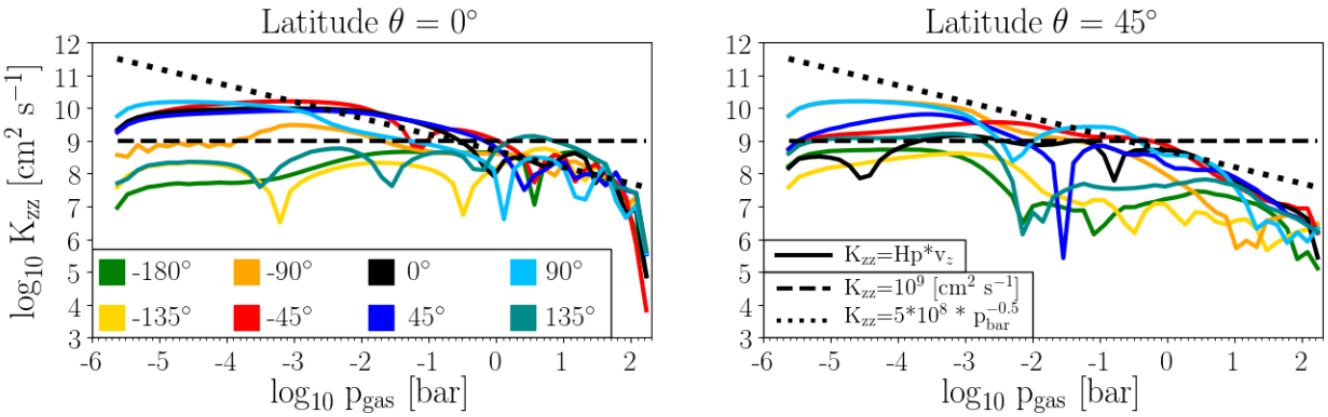

Fig. 10. Vertical diffusion coefficient, K_{zz}, calculated from various parameterisations: $K_{zz} = H_p v_z$, $K_{zz} = 10^9$ cm^{2}s^{-1}, and $K_{zz} = 5 \times 10^8 p^{-0.5}$ cm^2 s^{-1}. The representation $K_{zz} = f(p)$ is the same as derived in Parmentier et al. (2013).

on other ultra-hot Jupiters. For example, Kreidberg et al. (2018) concluded that a magnetic drag force is required to explain the phase curve of WASP-103b.

The dayside of WASP-18b reaches temperatures as high as 3500 K, which is too low to ionise the atomic hydrogen that dominates the dayside high-altitude atmosphere thermally (Fig. A.1). The nightside is completely neutral, and all elements appear in their first (neutral) state of ionisation. The dayside is composed of a partially ionised gas that has an electron number density comparable to and higher than Earth's ionosphere (10^6cm^{-3}). We therefore postulate that WASP-18b and other ultra-hot Jupiters such as WASP-121b, WASP-12b, WASP-103b, WASP-33b, Kepler-13Ab, Kepler 16b, KOI-13b, and MA-1b have an ionosphere on their daysides that stretches into the terminator regions. Planets to the right of the 20% line in Fig. 13 in Parmentier et al. (2018) will fall into this category.

The question now is whether the nightside would develop an ionosphere as well, for example as a result of scattered XUV photons from the host star (stellar XUV has a huge effect on the mass loss of small planets; e.g. King et al. 2018) or other high-energy irradiation from the interplanetary environment, for instance. It is reasonable to expect that external radiation increases the ionisation of the atmospheric gas in its upper high-altitude regions, similar to what has been shown for brown dwarfs. A considerable increase of the degree of ionisation results in a thin shell of an almost or fully ionised gas if the irradiation were comparable to the radiation field of the interstellar medium (Rodriguez-Barrera et al. 2018). Cosmic rays will not significantly contribute to the formation of an ionosphere because they are rather efficiently attenuated (Rimmer & Helling 2013).

5. Discussion

5.1. Element replenishment representations

The solution of the Navier–Stokes equations (or the Euler equations) in combination with a radiative transfer, gas-phase chemistry, element conservation, and cloud formation enables a parameter-free solution. Only material properties and numerical parameters remain to be adjusted. Not so in 1D. 1D approaches are numerically fast and can therefore be run on a high cadence as required, for example, in the retrieval approaches (e.g. Blecic et al. 2017). Our cloud formation model provides us with the tool that we need to predict cloud properties based on a fundamental understanding of microphysical processes such as cluster formation, frictional interaction, and surface reactions. We have demonstrated, however, that a replenishment mechanism is required to describe cloud formation in a 1D quasi-static atmospheric environment (Woitke & Helling 2004, Appendix A). Therefore, element replenishment is parameterised in 1D cloud simulations. Helling et al. (2008b) and Charnay et al. (2018) summarised the approaches applied in the literature for brown dwarfs and giant gas planets where $\tau_{\rm mix} \sim H_p(z)^2/K_{zz}$. Here, we test our classical approach of $K_{zz} = H_p v_z$ against a constant $K_{zz} = 10^9$ cm^{2}s^{-1} and a scaling with the local pressure $K_{zz} = 5 \times 10^8 p^{-0.5}$ with p in [bar]. The K_{zz} approach originates from modelling mixing as a diffusion process, and the $\tau_{\rm mix}$ approach models mixing as large-scale convection. The K_{zz} scaling with the local gas-pressure was derived from a 3D cloud-free GCM for HD209758b, which has a different temperature structure, as shown in Fig. 2. Figure 10 shows the variation in different parameterisations for the 1D profiles used here.

Figure 11 shows the nucleation rate and the mean cloud particle sizes for the three different K_{zz} parameterisations. Different profiles are shown in different colours, and the different K_{zz} cases are visualised by different line styles. The cloud results for the day- to nightside terminators remain rather unchanged for the three approaches we tested because the nucleation rates are very similar. For all other profiles, the largest differences occur to the approach that scales with the local gas pressure (dotted lines). The nucleation rate differs here by up to 4 orders of magnitude compared to the constant value (dashed lines). The consequence is that the mean particle sizes vary, but by only 1–1.5 orders of magnitudes at most in the inner, low-altitude cloud that is optically thick. The cloud particle load of the atmosphere reflects this as well.

While it is elusive to discuss which of the approaches could be called "correct", the comparison provides some idea about the uncertainties that are imposed by differences in K_{zz}. We have demonstrated this in terms of cloud particle load, $\rho_d/\rho_{\rm gas}$, and in terms of the C/O ratio (Fig. 12). The differences in the mixing/diffusion do not affect the results much at the equatorial cloud-forming terminator ($\phi = -90°$) and on the northern terminator at $\phi = 90°$ regarding $\rho_d/\rho_{\rm gas}$ and C/O. The largest uncertainties occur at the high altitudes of the cloudy atmosphere for the cloud itself and for the feedback on the gas phase.

We note that the three approaches give roughly the same answer, but the parameterised K_{zz} give a much smoother variation of parameters such as the particle size. This means that small-scale variations in the cloud properties are due to local

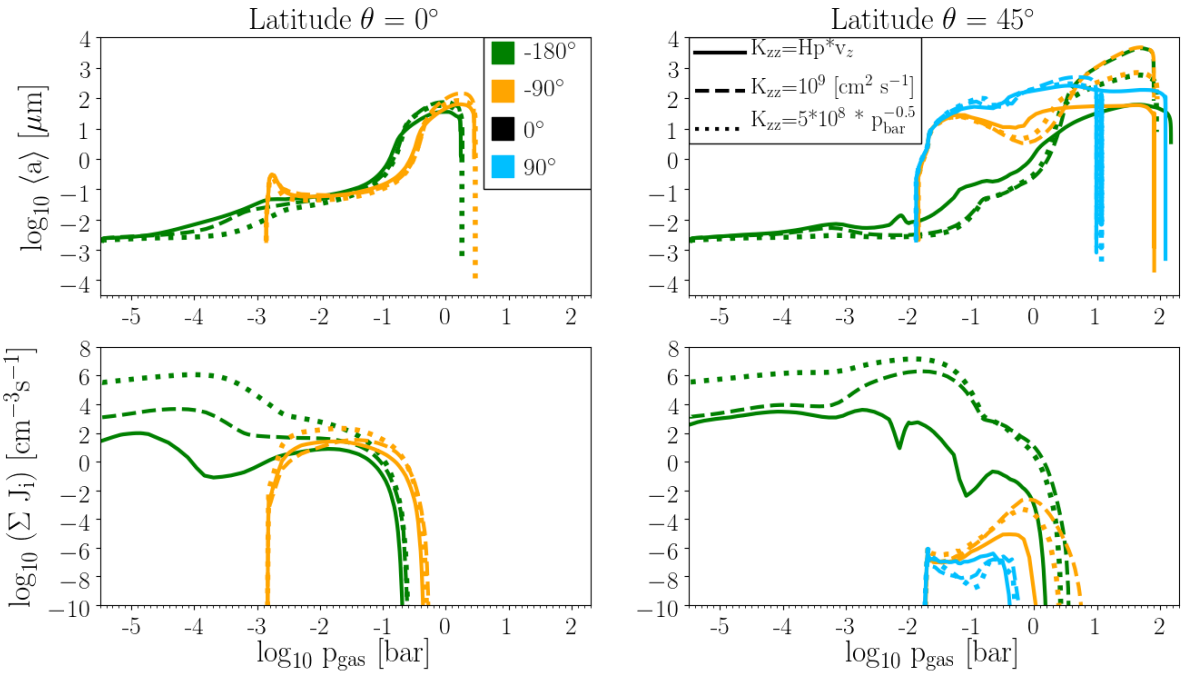

Fig. 11. Different element replenishment representations and the nucleation rate, $J_* = \Sigma J_i$, and the local mean particle size, $\langle a \rangle$, of WASP 18b.

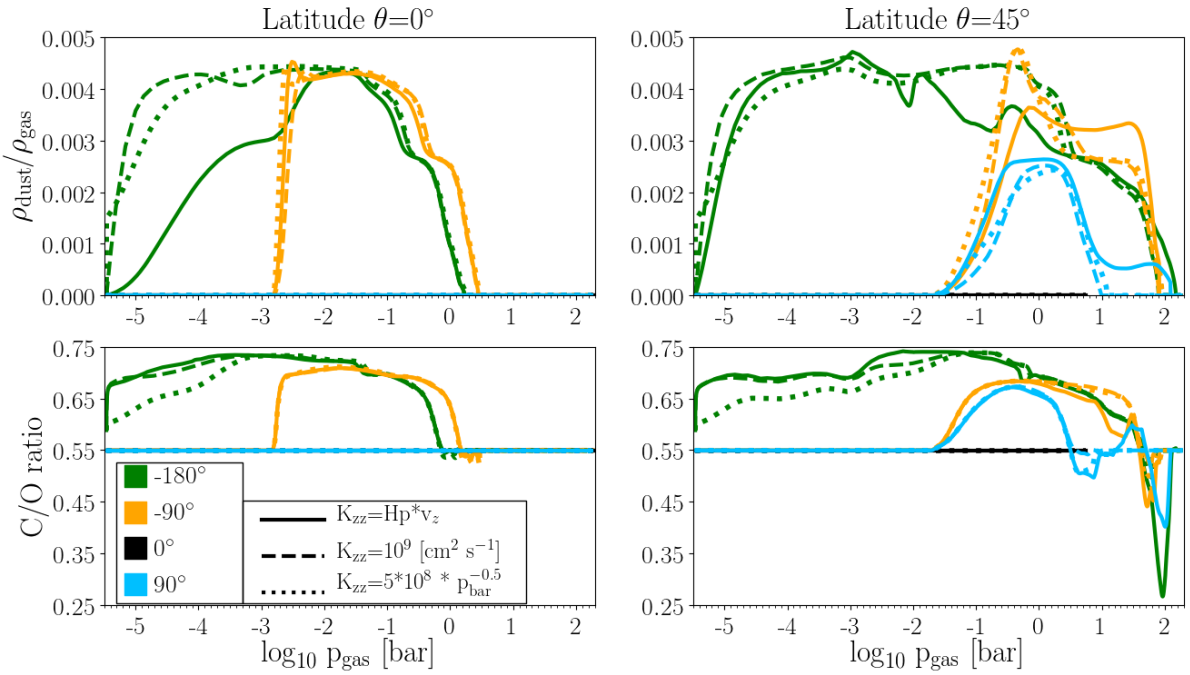

Fig. 12. Different element replenishment representations and global cloud properties of WASP-18b: ρ_d/ρ_{gas} (*top*) and C/O ratio (*bottom*).

variations of $K_{zz} = H_p v_z$ and might not be too realistic. Furthermore, horizontal mixing cannot be considered in the approach followed in this paper, but will homogenise the global element abundance and cloud particle distribution to a certain extent in the higher altitude regions where the gas pressure is low when the wind blows in the right direction (night → day) and thermally stability prevails. For example, the cloud particle size differences between the equator and the mid-latitudes and between the limb and the anti-stellar point would be smaller if the gas were supersaturated. For WASP-18b, the dayside will remain cloud free as no material achieves supersaturation for temperatures as high as >2200 K (Woitke et al. 2018). This condition worsens with decreasing pressure. It will be therefore essential to measure the atmospheric C/O on the day- and on the nightside in order to link the atmospheric C/O to the bulk C/O of extrasolar planets.

5.2. Comparing WASP-18b to HD 189733b and HD 209458b

Despite the limits of our approach, we can offer some general comparisons between the three giant gas planets that we have studied so far with respect to cloud formation and chemistry

feedback. This comparisons does not provide details on the atmosphere model as the 3D models for HD 189733b and HD 209458b take the clouds consistently into account for the gas-phase chemistry and for the radiative transfer, while this is not yet the case for WASP-18b.

WASP-18b with $T_{eq} \approx 2400$ K is far hotter than HD 189733b and HD 209458b with $T_{eq} \approx 1000$ K and $T_{eq} \approx 1500$ K, respectively, and its surface gravity is one order of magnitude higher. Figure 2 shows that despite these substantial differences in global parameters, the nightside of all three giant gas planets exhibits very comparable temperatures. All three planets also develop temperature inversions on their dayside (rather shallow in HD 209458b). In the low-pressure regions of the nightside profiles, WASP-18b has higher pressures for any given local gas temperature. Higher pressures enable condensation processes at higher temperatures as thermal stability expands into higher temperature regimes with increasing pressure.

The overall material composition of the cloud particles is very similar in all three planets, although differences do emerge in the details. The high-altitude atmosphere is dominated by Mg/Si/O-materials with ≈15% of Fe[s]. The nucleation species determine the composition of the thin uppermost cloud boundary. WASP-18b has a distinct SiO[s] layer where Mg/Si/O-materials have evaporated. This SiO[s] layer does not appear in HD 189733b and HD 209458b.

The overall mean particle sizes are comparable and span a similar range in all three planets. The actual height-dependent size distribution does vary between the planets. For example, the WASP-18b $\phi = -90°$ terminator shows only very small changes of cloud particles sizes with height compared to all other sampled profiles. Here the material matrix is dominated by SiO[s] over most of the cloud volume, except for the cloud top, where distinct layers of Fe[s] and $CaTiO_2$[s] appear.

The total vertical cloud extension reaches farther into the low-pressure atmosphere on WASP-18b despite having a surface gravity that is one order of magnitude higher than that of HD 189733b. The clouds of HD 209458b reach into the lowest pressure regimes: the upper nightside cloud boundary is located at $p_{gas} \approx 10^{-5.5}$ bar on WASP-18b, at $p_{gas} \approx 10^{-4.2}$ bar on HD 189733b, and at $p_{gas} \approx 10^{-7} \ldots 10^{-5}$ bar on HD 209458b (compare Fig. 4 and Fig. 8 in Helling et al. 2016). Our test of mixing prescriptions in Sect. 5.1 suggests that the upper cloud boundary is not affected by mixing here and is therefore determined by the local thermodynamic conditions.

6. Conclusion

WASP-18b provides us with a laboratory for studying the atmosphere chemistry of ultra-hot Jupiters that have very hot days and cold nights. Not all constituents of hot Jupiters are in the gas phase, and cloud formation strongly affects the chemistry on the nightside and on the day- to nightside terminators. The WASP-18b dayside is hot enough to thermally dissociate H_2, and the elements Na, K, Ca, Ti, and Al as well as Fe, Mg, and Si, but to a lesser degree. VO, TiO, and H_2O are not among the most abundant gas-phase species on the dayside, which is in line with the non-detection in HST secondary eclipse observations. TiO and H_2O are important for gas pressures above 10^{-2} bar on the dayside. The low-density regime of the dayside has CO but also atomic species such as Si and S, and ions such as Na^+, Ca^+, and K^+. The low-pressure regime of the terminator gas-phase chemistry is made of bi-atomic molecules such as CO, SiO, and TiO and atoms such as Fe and Mg. Our other findings are listed below.

- WASP-18b has two very different sides: the nightside is cloudy and elements depleted, the dayside is cloud-free and forms a thermal ionosphere that reaches deep into the atmosphere.
- The largest cloud particles form at the $\phi = -90°$ (west) day/night terminator, and super-rotation causes a cloud-free $\phi = 90°$ (east) day/night terminator.
- Clouds become more extended towards the west of the nightside. Clouds are located farther inside the atmosphere and are less extended at the limbs than at the nightside.
- The cloud particle load (dust-to-gas ratio ρ_d/ρ_{gas}) is rather homogeneous of the order of 10^{-3} despite the large temperature difference in the cloud-forming regions of WASP-18b.
- Element enrichment occurs deep inside the atmosphere, and the observable layers appear depleted in all elements that participate in cloud formation.
- At the dayside, where no cloud formation occurs, the atmospheric C/O is constant and remains at its undepleted value (here: solar). At the nightside, C/O is roughly constant but enhanced (C/O∼0.7) within the photosphere. At the limbs, the C/O ratio varies vertically from 0.7 to 0.5 within the layers that are probed by transmission spectroscopy. Cloud formation does enhance the C/O in general.
- The cloud particles are made of a mix of materials that changes depending on the local temperature in the atmosphere. The mix is predominantly made of O-binding minerals, smaller oxides, or iron, but 5–10% of carbon can occasionally be mixed in. The cloud particle sizes change with height and location.
- The molecular number densities vary by orders of magnitudes between the day- and the nightside and the limbs.

Acknowledgements. Jacob Arcangeli is acknowledged for helpful discussions on this manuscript.

References

Adibekyan, V., Gonçalves da Silva, H. M., Sousa, S. G., et al. 2017, Astrophysics, 60, 325
Alessi, M., & Pudritz, R. E. 2018, MNRAS, 478, 2599
Arcangeli, J., Désert, J.-M., Line, M. R., et al. 2018, ApJ, 855, L30
Arkhipova, V. P., Parthasarathy, M., Ikonnikova, N. P., et al. 2018, MNRAS, 481, 3935
Asplund, M., Grevesse, N., & Sauval, A. J. 2005, in Cosmic Abundances as Records of Stellar Evolution and Nucleosynthesis, eds. T. G. Barnes, III, & F. N. Bash, ASP Conf. Ser., 336, 25
Asplund, M., Grevesse, N., Sauval, A. J., & Scott, P. 2009, ARA&A, 47, 481
Bedell, M., Bean, J. L., Melendez, J., et al. 2018, ApJ, 865, 68
Bell, T. J., & Cowan, N. B. 2018, ApJ, 857, L20
Blecic, J., Dobbs-Dixon, I., & Greene, T. 2017, ApJ, 848, 127
Bond, J. C., O'Brien, D. P., & Lauretta, D. S. 2010, ApJ, 715, 1050
Burningham, B., Marley, M. S., Line, M. R., et al. 2017, MNRAS, 470, 1177
Charnay, B., Bézard, B., Baudino, J.-L., et al. 2018, ApJ, 854, 172
Dobbs-Dixon, I., & Agol, E. 2013, MNRAS, 435, 3159
Eistrup, C., Walsh, C., & van Dishoeck, E. F. 2018, A&A, 613, A14
Fossati, L., Ayres, T. R., Haswell, C. A., et al. 2014, Ap&SS, 354, 21
Freedman, R. S., Marley, M. S., & Lodders, K. 2008, ApJS, 174, 504
Freedman, R. S., Lustig-Yaeger, J., Fortney, J. J., et al. 2014, ApJS, 214, 25
Fulle, M., Colangeli, L., Agarwal, J., et al. 2010, A&A, 522, A63
Gandhi, S., & Madhusudhan, N. 2018, MNRAS, 474, 271
Goumans, T. P. M., & Bromley, S. T. 2012, MNRAS, 420, 3344
Grevesse, N., Asplund, M., & Sauval, A. J. 2007, Space Sci. Rev., 130, 105
Hellier, C., Anderson, D. R., Collier Cameron, A., et al. 2009, Nature, 460, 1098
Helling, C., & Woitke, P. 2006, A&A, 455, 325
Helling, C., & Rietmeijer, F. J. M. 2009, Int. J. Astrobiol., 8, 3
Helling, C., & Fomins, A. 2013, Phil. Trans. R. Soc. London, Ser. A, 371, 10581
Helling, C., & Casewell, S. 2014, A&ARv, 22, 80
Helling, C., Winters, J. M., & Sedlmayr, E. 2000, A&A, 358, 651

Helling, C., Woitke, P., & Thi, W.-F. 2008a, A&A, 485, 547
Helling, C., Ackerman, A., Allard, F., et al. 2008b, MNRAS, 391, 1854
Helling, C., Woitke, P., Rimmer, P. B., et al. 2014, Life, 4, 142
Helling, C., Lee, G., Dobbs-Dixon, I., et al. 2016, MNRAS, 460, 855
Helling, C., Tootill, D., Woitke, P., & Lee, G. 2017, A&A, 603, A123
Iro, N., & Maxted, P. F. L. 2013, Icarus, 226, 1719
Jeong, K. S., Chang, C., Sedlmayr, E., & Sülzle, D. 2000, J. Phys. B At. Mol. Phys., 33, 3417
Kataria, T., Showman, A. P., Fortney, J. J., et al. 2015, ApJ, 801, 86
Kataria, T., Sing, D. K., Lewis, N. K., et al. 2016, ApJ, 821, 9
King, G. W., Wheatley, P. J., Salz, M., et al. 2018, MNRAS, 478, 1193
Koll, D. D. B., & Komacek, T. D. 2018, ApJ, 853, 133
Komacek, T. D., & Showman, A. P. 2016, ApJ, 821, 16
Kopparapu, R. k., Kasting, J. F., & Zahnle, K. J. 2012, ApJ, 745, 77
Kreidberg, L., Line, M. R., Parmentier, V., et al. 2018, AJ, 156, 17
Langland-Shula, L. E., & Smith, G. H. 2011, Icarus, 213, 280
Lee, G., Helling, C., Giles, H., & Bromley, S. T. 2015a, A&A, 575, A11
Lee, G., Helling, C., Dobbs-Dixon, I., & Juncher, D. 2015b, A&A, 580, A12
Lee, G. K. H., Blecic, J., & Helling, C. 2018, A&A, 614, A126
Lewis, N. K., Parmentier, V., Kataria, T., et al. 2017, AJ, submitted [arXiv:1706.00466]
Line, M. R., Liang, M. C., & Yung, Y. L. 2010, ApJ, 717, 496
Longstaff, E. S., Casewell, S. L., Wynn, G. A., Maxted, P. F. L., & Helling, C. 2017, MNRAS, 471, 1728
Lothringer, J. D., Barman, T., & Koskinen, T. 2018, ApJ, 866, 27
Marley, M. S., Saumon, D., Fortney, J. J., et al. 2017, AAS Meeting Abstracts, 230, 315.07
Mayne, N. J., Baraffe, I., Acreman, D. M., et al. 2014, A&A, 561, A1
Moses, J. I., Visscher, C., Fortney, J. J., et al. 2011, ApJ, 737, 15
Moses, J. I., Line, M. R., Visscher, C., et al. 2013, ApJ, 777, 34
Nuth, J. A., III, & Ferguson, F. T. 2006, ApJ, 649, 1178
Nymeyer, S., Harrington, J., Hardy, R. A., et al. 2011, ApJ, 742, 35
Parmentier, V., Showman, A. P., & Lian, Y. 2013, A&A, 558, A91
Parmentier, V., Fortney, J. J., Showman, A. P., Morley, C., & Marley, M. S. 2016, ApJ, 828, 22
Parmentier, V., Line, M. R., Bean, J. L., et al. 2018, A&A, 617, A110
Plane, J. M. C. 2013, Phil. Trans. R. Soc. London, Ser. A, 371, 20335
Ramstedt, S., Maercker, M., Olofsson, G., Olofsson, H., & Schöier, F. L. 2011, A&A, 531, A148
Rimmer, P. B., & Helling, C. 2013, ApJ, 774, 108
Rodríguez-Barrera, M. I., Helling, C., Stark, C. R., & Rice, A. M. 2015, MNRAS, 454, 3977
Rodriguez-Barrera, M. I., Helling, C., & Wood, K. 2018, ArXiv e-prints [arXiv:1804.09054]
Rogers, T. M. 2017, Nat. Astron., 1, 0131
Rogers, T. M., & Showman, A. P. 2014, ApJ, 782, L4
Roman, M., & Rauscher, E. 2017, ApJ, 850, 17
Schwartz, J. C., & Cowan, N. B. 2015, MNRAS, 449, 4192
Sharp, C. M., & Huebner, W. F. 1990, ApJS, 72, 417
Sheppard, K. B., Mandell, A. M., Tamburo, P., et al. 2017, ApJ, 850, L32
Showman, A. P., Fortney, J. J., Lian, Y., et al. 2009, ApJ, 699, 564
Sicilia-Aguilar, A., Oprandi, A., Froebrich, D., et al. 2017, A&A, 607, A127
Skemer, A. J., Morley, C. V., Zimmerman, N. T., et al. 2016, ApJ, 817, 166
Southworth, J., Hinse, T. C., Dominik, M., et al. 2009, ApJ, 707, 167
Suárez-Andrés, L., Israelian, G., González Hernández, J. I., et al. 2018, A&A, 614, A84
Triaud, A. H. M. J., Collier Cameron, A., Queloz, D., et al. 2010, A&A, 524, A25
Venot, O., Hébrard, E., Agúndez, M., et al. 2012, A&A, 546, A43
Visscher, C., Lodders, K., & Fegley, Jr. B. 2006, ApJ, 648, 1181
Visscher, C., Lodders, K., & Fegley, Jr. B. 2010, ApJ, 716, 1060
Wakeford, H. R., Visscher, C., Lewis, N. K., et al. 2017, MNRAS, 464, 4247
Woitke, P., & Helling, C. 2003, A&A, 399, 297
Woitke, P., & Helling, C. 2004, A&A, 414, 335
Woitke, P., Helling, C., Hunter, G. H., et al. 2018, A&A, 614, A1
Zahnle, K., Marley, M. S., Freedman, R. S., Lodders, K., & Fortney, J. J. 2009, ApJ, 701, L20
Zhang, X., & Showman, A. P. 2018, ApJ, 866, 1
Zhou, G., Bayliss, D. D. R., Kedziora-Chudczer, L., et al. 2015, MNRAS, 454, 3002

Appendix A: Details on chemical composition

Table A.1. Solar element abundances, ϵ^0 (Asplund et al. 2009), and solar mineral ratios $[X/Si] = \epsilon^0_X/\epsilon^0_{Si}$, Si/O, and C/O.

	ϵ^0		$\epsilon^0_X/\epsilon^0_{Si,O}$
H	1.000	H/Si	3.0902×10^4
He	8.511×10^{-2}	He/Si	2.6301e3
Li	1.122×10^{-11}	Li/Si	3.4672×10^{-7}
C	2.692×10^{-4}	C/Si	8.3189
N	6.761×10^{-5}	N/Si	2.0893
O	4.898×10^{-4}	O/Si	1.5136e1
Na	1.738×10^{-6}	Na/Si	5.3708×10^{-2}
Mg	3.981×10^{-5}	Mg/Si	1.2302
Al	2.818×10^{-6}	Al/Si	8.7082×10^{-2}
S	1.318×10^{-5}	S/Si	0.40729
Cl	3.162×10^{-7}	Cl/Si	9.7713×10^{-3}
K	1.072×10^{-7}	K/Si	3.3127×10^{-3}
Ca	2.188×10^{-6}	Ca/Si	6.7614×10^{-2}
Ti	8.913×10^{-8}	Ti/Si	2.7543×10^{-3}
Fe	3.162×10^{-5}	Fe/Si	9.7713×10^{-1}
Si	3.236×10^{-5}	Si/Si	1
		C/O	0.5495
		Si/O	6.6067×10^{-2}

Notes. Bedell et al. (2018) and Bond et al. (2010) cite Mg/Si = 1.05 based on the element abundance data from Asplund et al. (2005) with $\epsilon^0_{Mg} = 7.53$.

Here we provide the detailed composition of the gas phase in chemical equilibrium for the eight profiles probed at the equator and in the northern hemisphere. We note that the 3D atmosphere models are north-south symmetric such that the southern hemisphere shows the same behaviour as the northern hemisphere.

We first provide an overview of the change in the abundances of the dominating molecular species (Fig. 8) along the equator on the day- and nightside. Figures A.2–A.12 detail the chemical gas-phase composition with respect to the individual elements H, O, Al, C, Ca, Fe, Mg, Si, S, and Ti. Each of these plots (Figs A.2–A.12) also shows an element ratio (mineralogical ratios) at the right axis (Al/Si, C/O, Ca/Si, Fe/Si, Mg/Si, Si/O, S/Si, and Ti/Si).

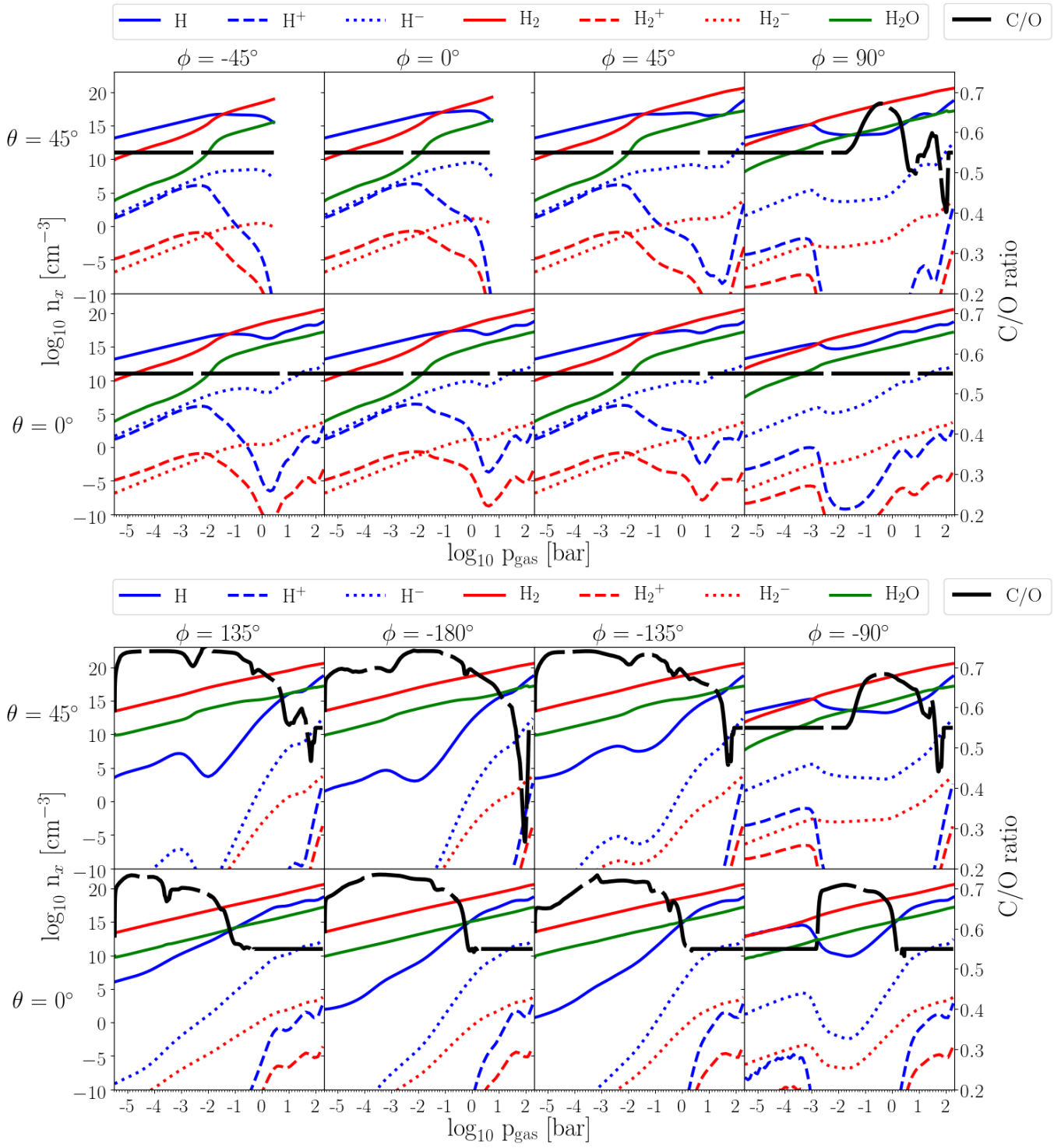

Fig. A.1. Number densities, log n_x [cm^{-3}], of H-binding gas-species (colour-coded, left axis). The C/O is overplotted and shows where cloud affects the atmosphere (black long-dashed line, right axis).

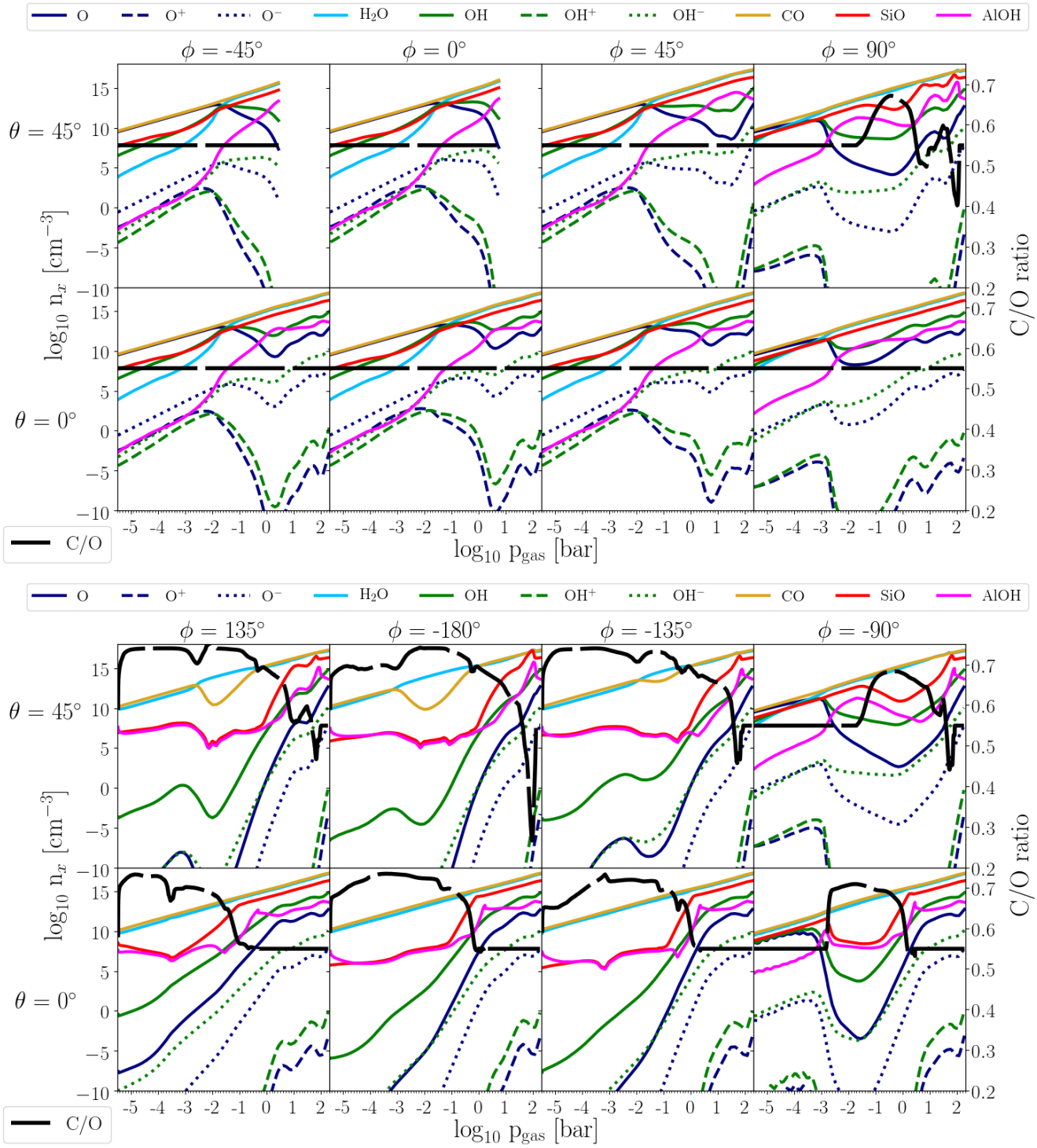

Fig. A.2. Number densities, log n_x [cm^{-3}], of O-binding gas-species (colour-coded, left axis). The C/O is overplotted and shows where cloud affects the atmosphere (black long-dashed line, right axis).

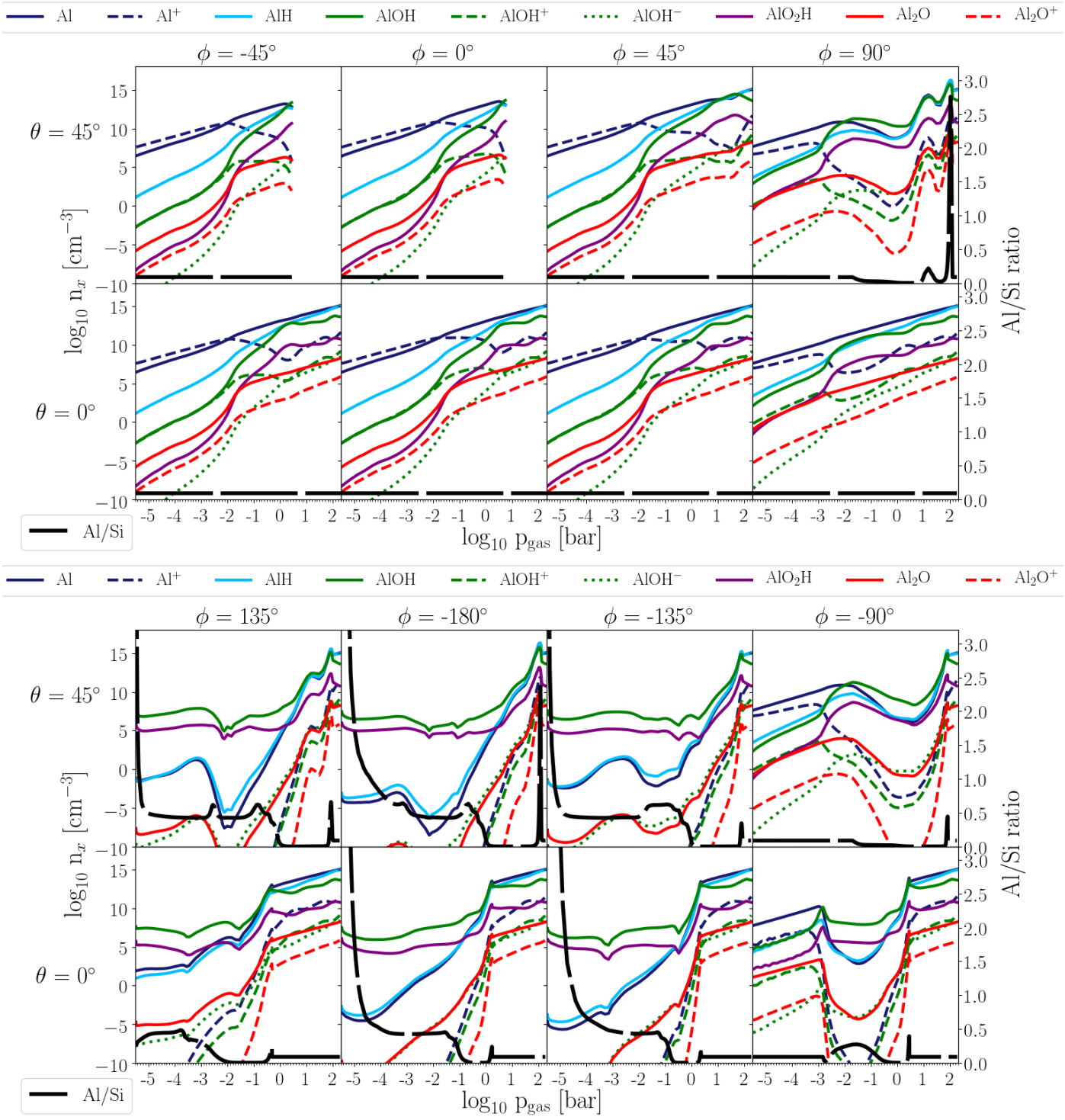

Fig. A.3. Number densities, log n_x [cm^{-3}], of aluminum binding gas-species (colour-coded, left axis). The Al/Si ratio is overplotted and shows where cloud affects the atmosphere (black long-dashed line, right axis).

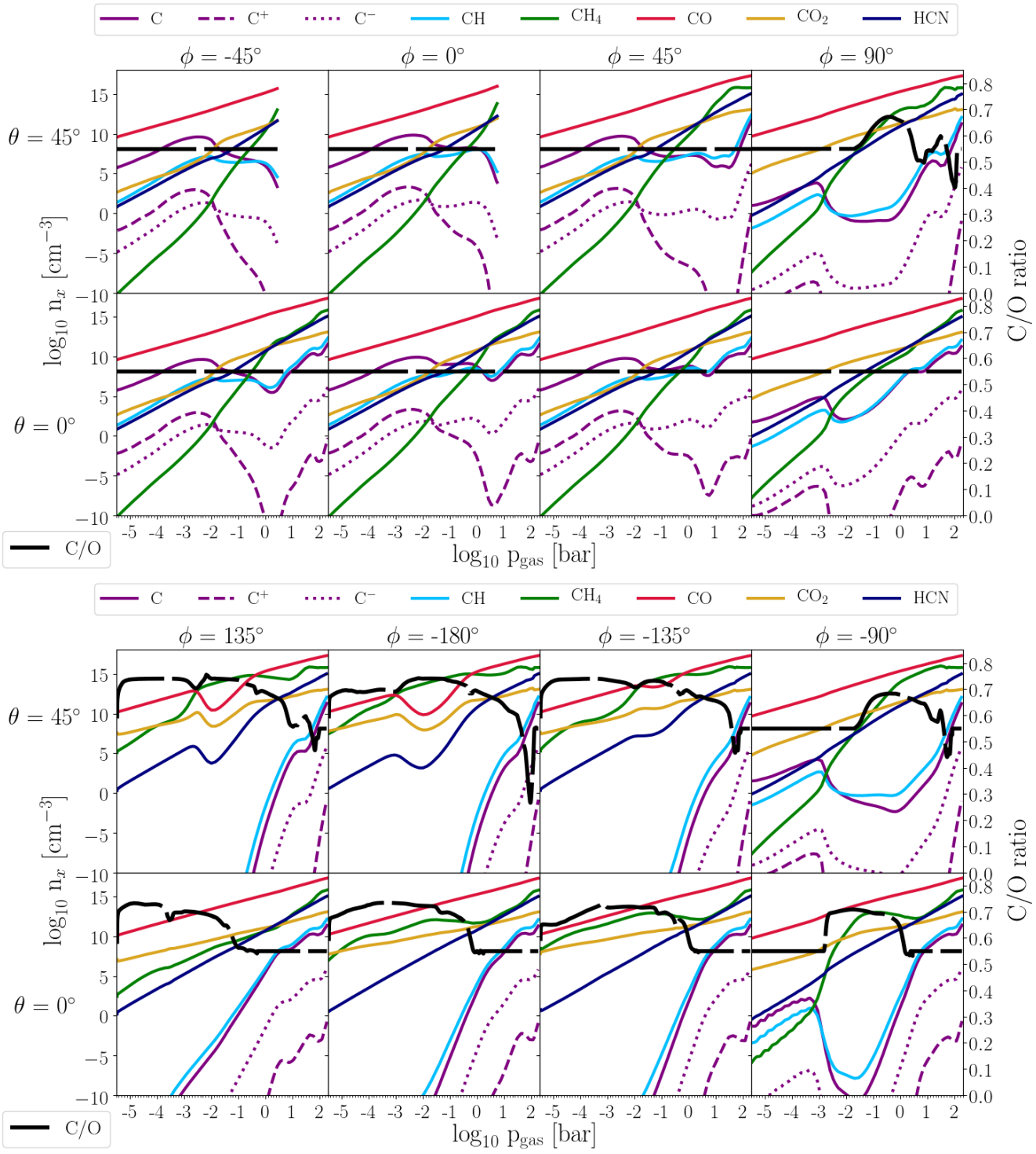

Fig. A.4. Number densities, log n_x [cm^{-3}], of carbon-binding gas species (colour-coded, left axis). The C/O is overplotted and shows where cloud affects the atmosphere (black long-dashed line, right axis).

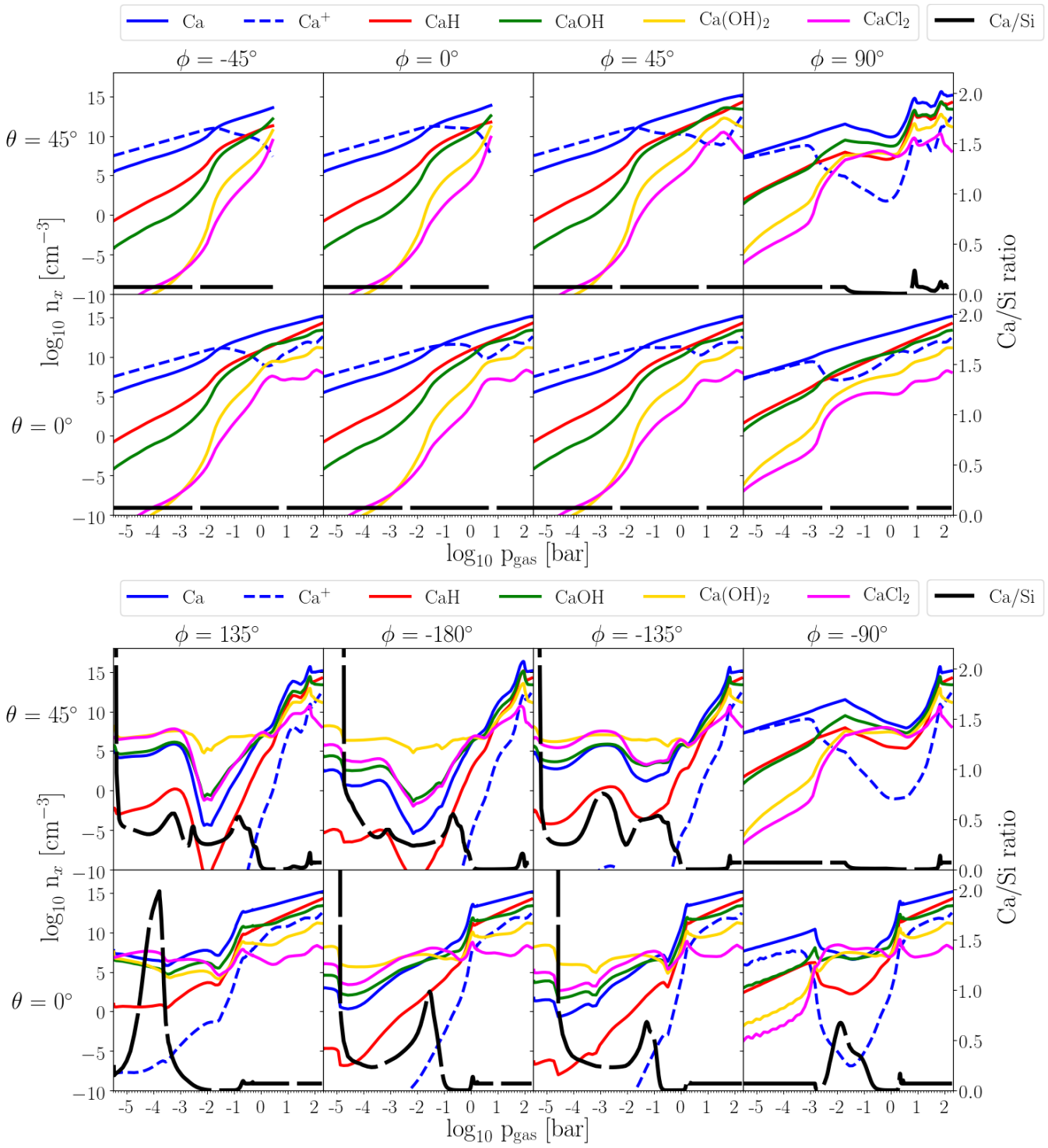

Fig. A.5. Number densities, log n_x [cm^{-3}], of Ca-binding gas species (colour-coded, left axis). The Ca/Si ratio is overplotted and shows where cloud affects the atmosphere (black long-dashed line, right axis).

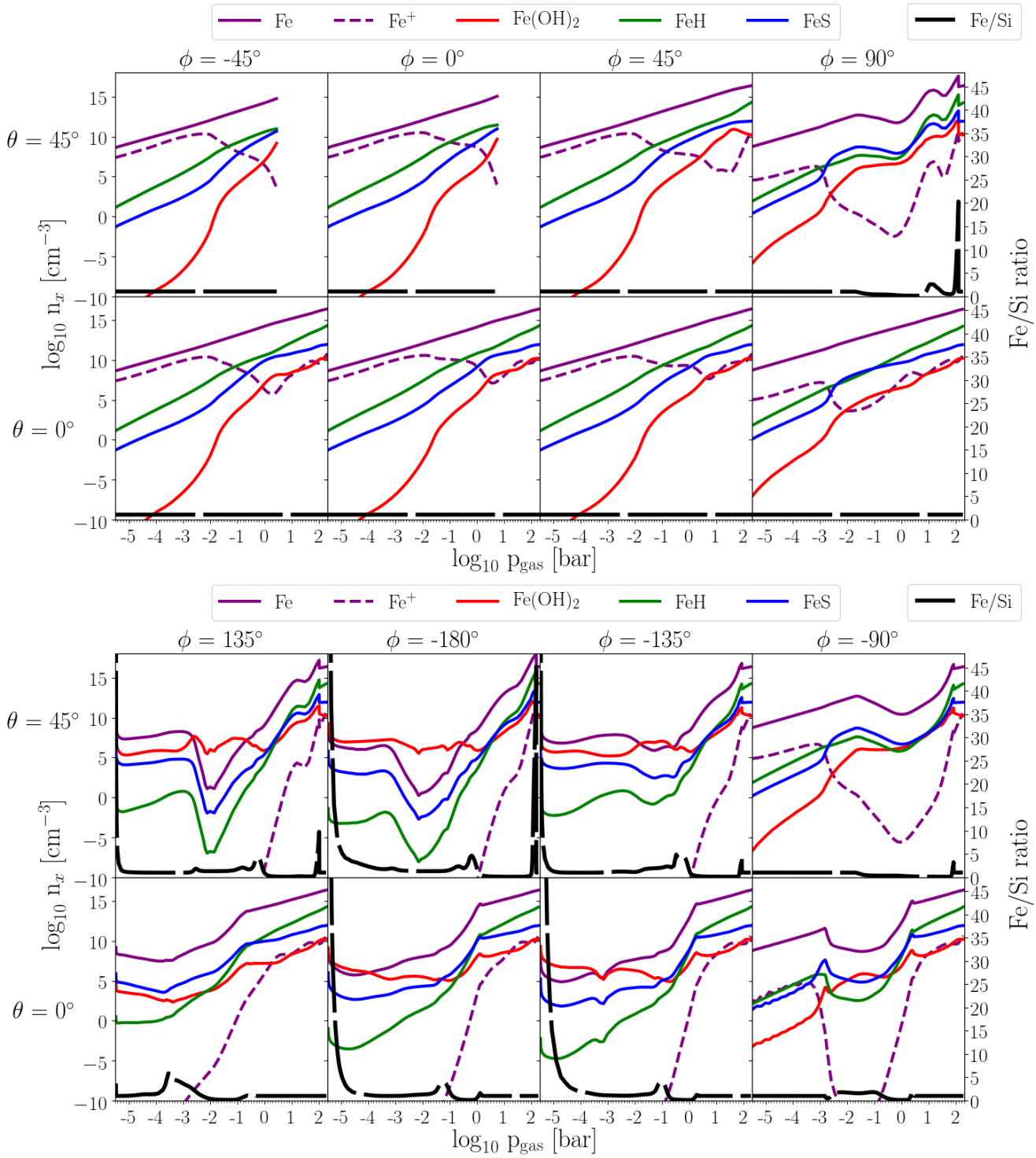

Fig. A.6. Number densities, log n_x [cm^{-3}], of Fe-binding gas species (colour-coded, left axis). The Fe/Si ratio is overplotted and shows where cloud affects the atmosphere (black long-dashed line, right axis).

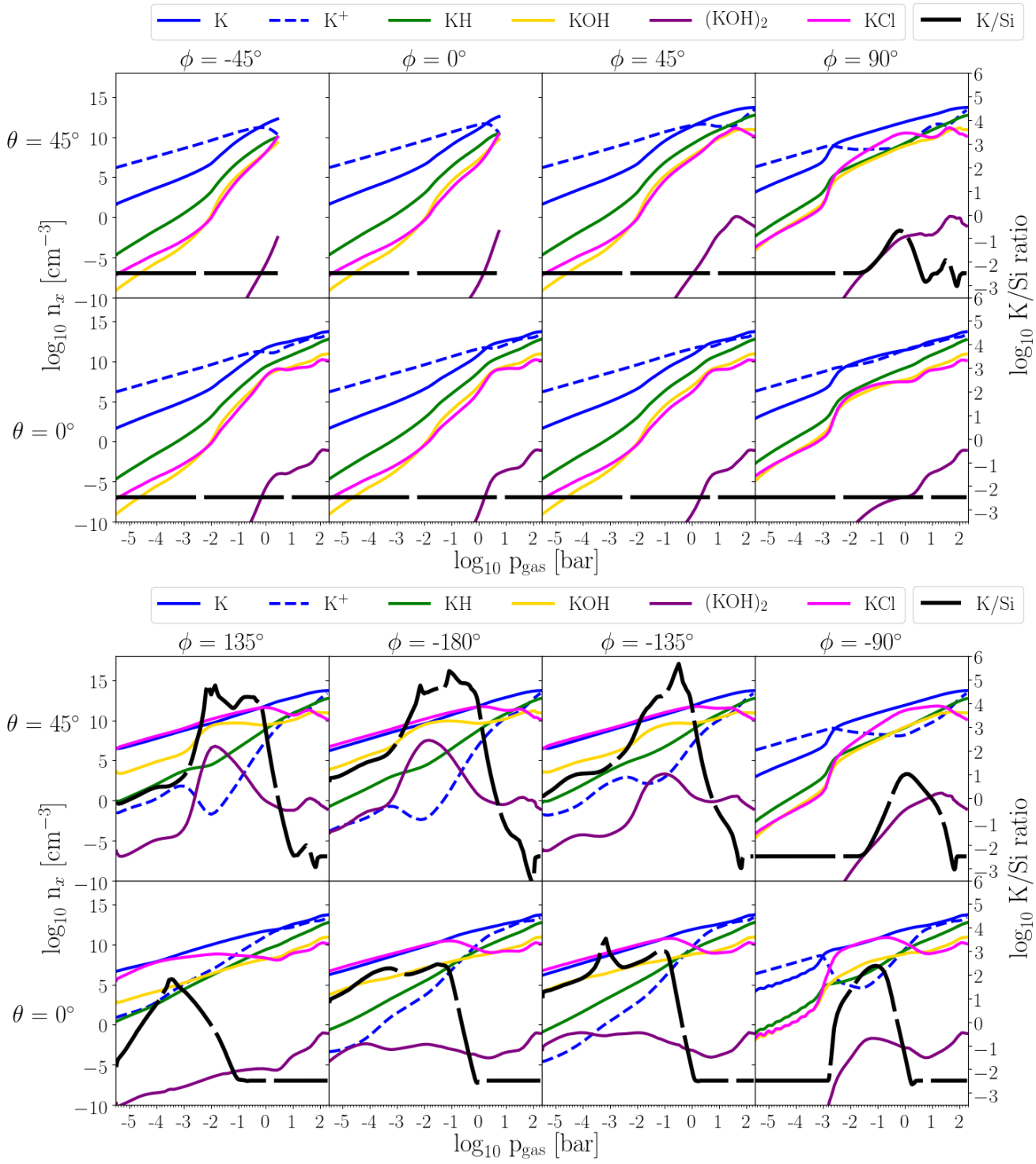

Fig. A.7. Number densities, log n_x [cm^{-3}], of K-binding gas species (colour-coded, left axis). The log(K/Si) ratio is overplotted and shows where cloud affects the atmosphere (black long-dashed line, right axis).

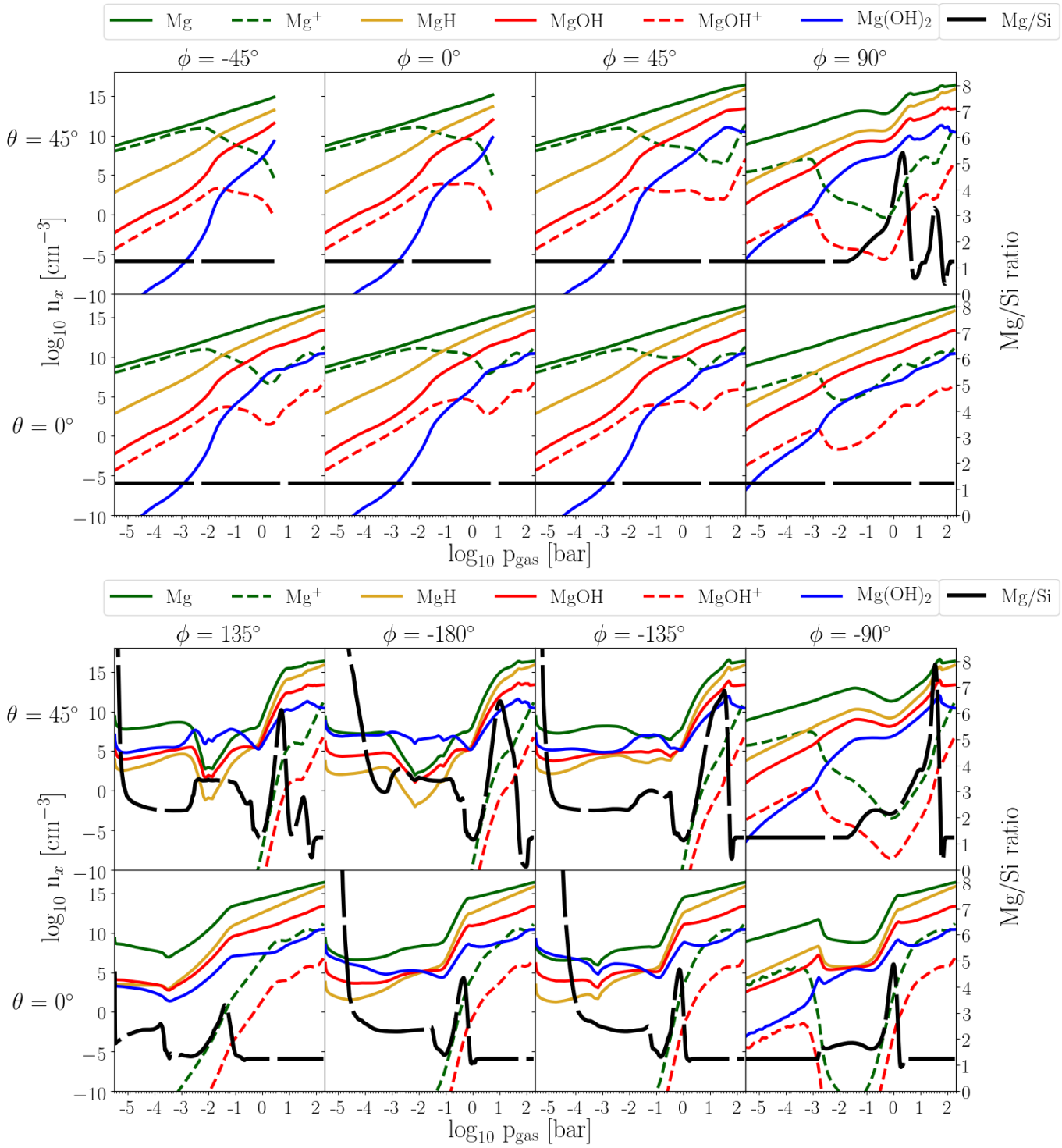

Fig. A.8. Number densities, log n_x [cm^{-3}], of Mg-binding gas species (colour-coded, left axis). The Mg/Si ratio is overplotted and shows where cloud affects the atmosphere (black long-dashed line, right axis).

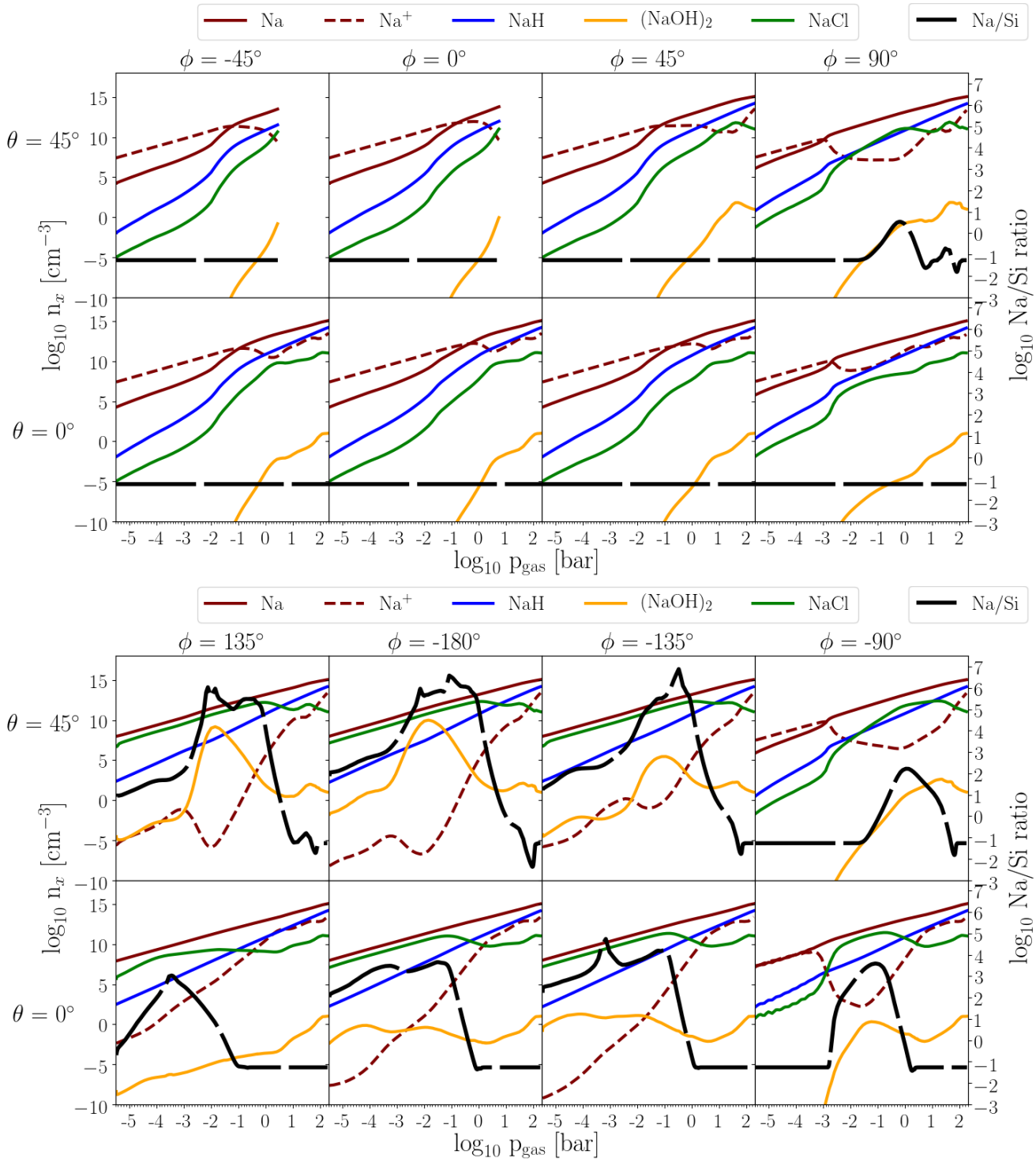

Fig. A.9. Number densities, log n_x [cm^{-3}], of Na-binding gas species (colour-coded, left axis). The log(Na/Si) ratio is overplotted and shows where cloud affects the atmosphere (black long-dashed line, right axis).

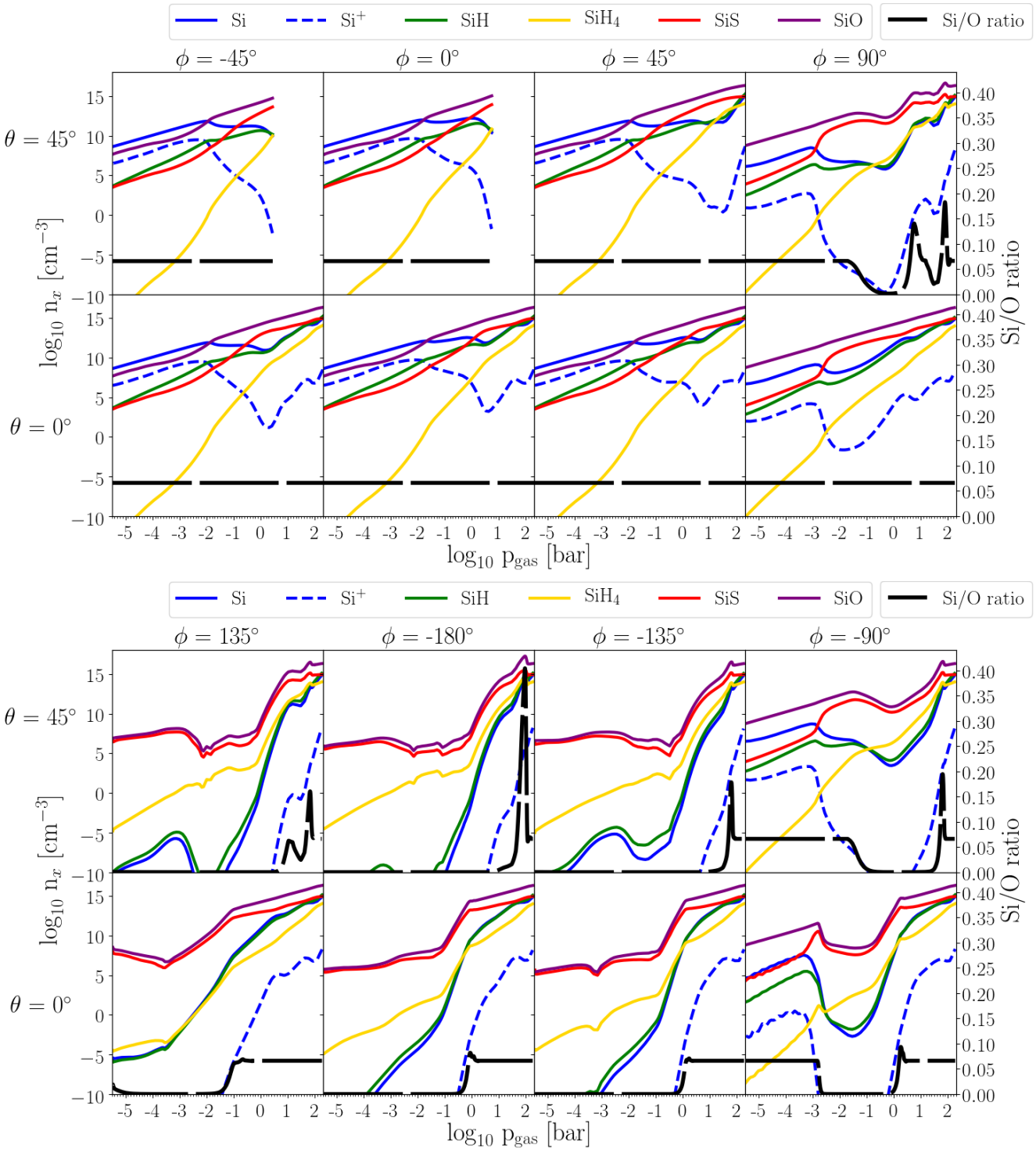

Fig. A.10. Number densities, log n_x [cm^{-3}], of Si-binding gas species (colour-coded, left axis). The Si/O ratio is overplotted and shows where cloud affects the atmosphere (black long-dashed line, right axis).

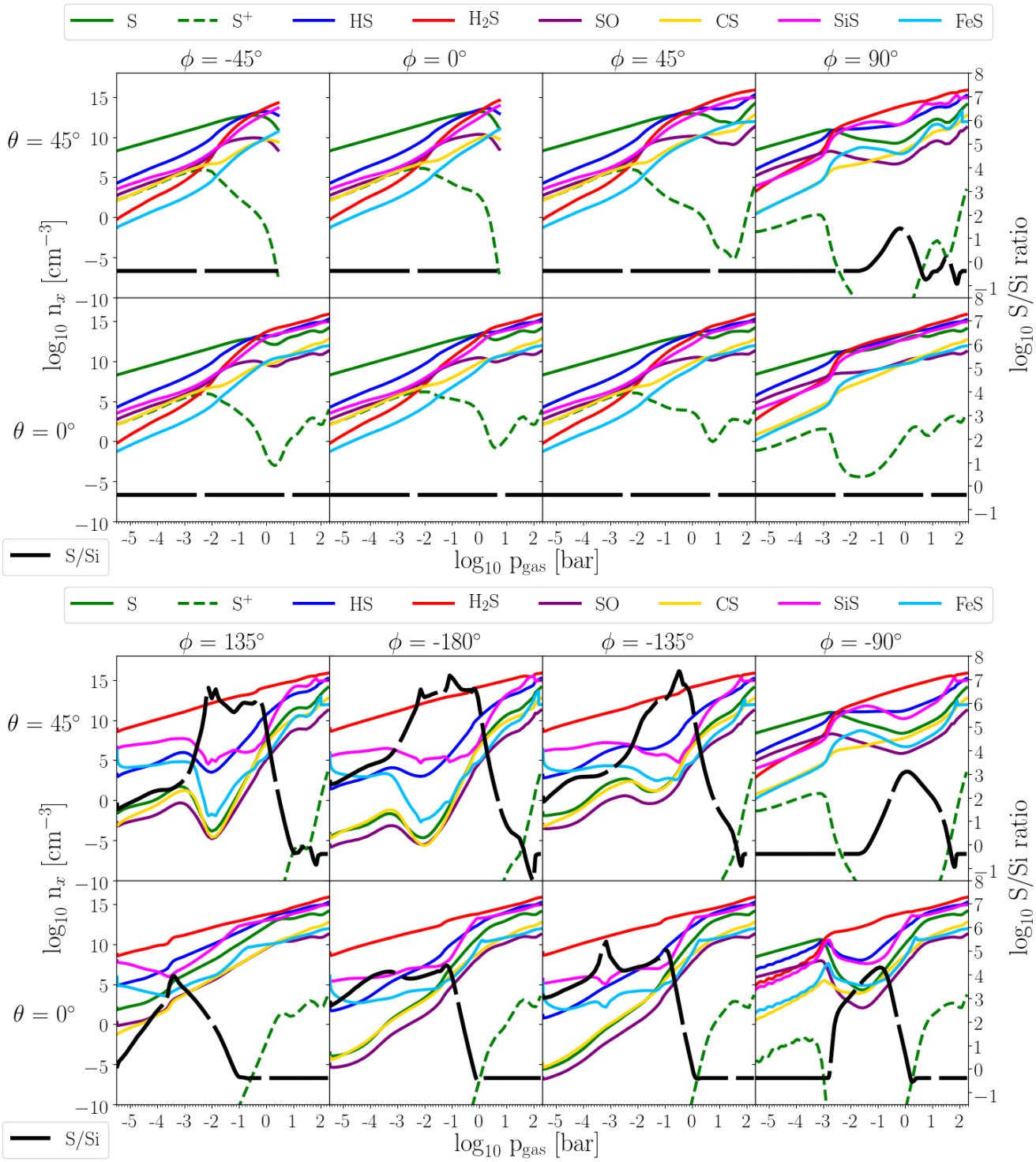

Fig. A.11. Number densities, log n_x [cm^{-3}], of S-binding gas species (colour-coded, left axis). The log(S/Si) ratio is overplotted and shows where cloud affects the atmosphere (black long-dashed line, right axis).

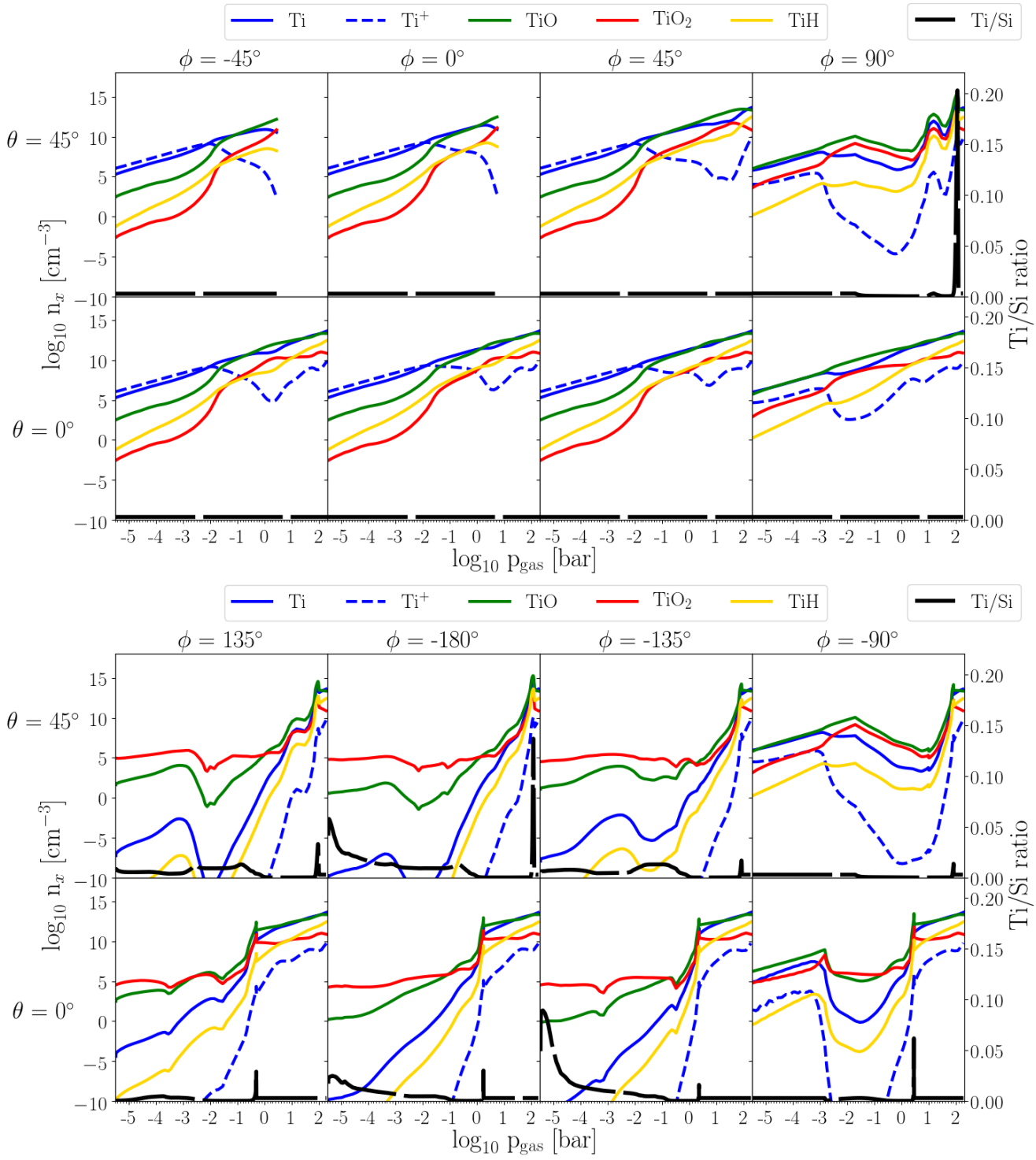

Fig. A.12. Number densities, log n_x [cm^{-3}], of Ti-binding gas species (colour-coded, left axis). The Ca/Si ratio is overplotted and shows where cloud affects the atmosphere (black long-dashed line, right axis).

Appendix B: Input details

Table B.1. Chemical surface reactions r assumed to form the solid materials s.

Index r	Solid s	Surface reaction	Key species
1	TiO_2[s]	$TiO_2 \longrightarrow TiO_2$[s]	TiO_2
2	rutile	$Ti + 2\,H_2O \longrightarrow TiO_2$[s] $+ 2\,H_2$	Ti
3	(1)	$TiO + H_2O \longrightarrow TiO_2$[s] $+ H_2$	TiO
4		$TiS + 2\,H_2O \longrightarrow TiO_2$[s] $+ H_2S + H_2$	TiS
5	SiO_2[s]	$SiH + 2\,H_2O \longrightarrow SiO_2$[s] $+ 2\,H_2 + H$	SiH
6	silica	$SiO + H_2O \longrightarrow SiO_2$[s] $+ H_2$	SiO
7	(3)	$SiS + 2\,H_2O \longrightarrow SiO_2$[s] $+ H_2S + H_2$	SiS
8	SiO[s]	$SiO \longrightarrow SiO$[s]	SiO
9	silicon mono-oxide	$2\,SiH + 2\,H_2O \longrightarrow 2\,SiO$[s] $+ 3\,H_2$	SiH
10	(2)	$SiS + H_2O \longrightarrow SiO$[s] $+ H_2S$	SiS
11	Fe[s]	$Fe \longrightarrow Fe$[s]	Fe
12	solid iron	$FeO + H_2 \longrightarrow Fe$[s] $+ H_2O$	FeO
13	(1)	$FeS + H_2 \longrightarrow Fe$[s] $+ H_2S$	FeS
14		$Fe(OH)_2 + H_2 \longrightarrow Fe$[s] $+ 2\,H_2O$	$Fe(OH)_2$
15		$2\,FeH \longrightarrow 2\,Fe$[s] $+ H_2$	FeH
16	FeO[s]	$FeO \longrightarrow FeO$[s]	FeO
17	iron (II) oxide	$Fe + H_2O \longrightarrow FeO$[s] $+ H_2$	Fe
18	(3)	$FeS + H_2O \longrightarrow FeO$[s] $+ H_2S$	FeS
19		$Fe(OH)_2 \longrightarrow FeO$[s] $+ H_2$	$Fe(OH)_2$
20		$2\,FeH + 2\,H_2O \longrightarrow 2\,FeO$[s] $+ 3\,H_2$	FeH
21	FeS[s]	$FeS \longrightarrow FeS$[s]	FeS
22	iron sulphide	$Fe + H_2S \longrightarrow FeS$[s] $+ H_2$	Fe
23	(3)	$FeO + H_2S \longrightarrow FeS$[s] $+ H_2O$	min{FeO, H_2S}
24		$Fe(OH)_2 + H_2S \longrightarrow FeS$[s] $+ 2\,H_2O$	min{$Fe(OH)_2$, H_2S}
25		$2\,FeH + 2\,H_2S \longrightarrow 2\,FeS$[s] $+ 3\,H_2$	min{FeH, H_2S}
26	Fe_2O_3[s]	$2\,Fe + 3\,H_2O \longrightarrow Fe_2O_3$[s] $+ 3\,H_2$	$\frac{1}{2}$Fe
27	iron (III) oxide	$2\,FeO + H_2O \longrightarrow Fe_2O_3$[s] $+ H_2$	$\frac{1}{2}$FeO
28	(3)	$2\,FeS + 3\,H_2O \longrightarrow Fe_2O_3$[s] $+ 2\,H_2S + H_2$	$\frac{1}{2}$FeS
29		$2\,Fe(OH)_2 \longrightarrow Fe_2O_3$[s] $+ H_2O + H_2$	$\frac{1}{2}$$Fe(OH)_2$
30		$2\,FeH + 3\,H_2O \longrightarrow Fe_2O_3$[s] $+ 4\,H_2$	$\frac{1}{2}$FeH
31	MgO[s]	$Mg + H_2O \longrightarrow MgO$[s] $+ H_2$	Mg
32	periclase	$2\,MgH + 2\,H_2O \longrightarrow 2\,MgO$[s] $+ 3\,H_2$	$\frac{1}{2}$MgH
33	(3)	$2\,MgOH \longrightarrow 2\,MgO$[s] $+ H_2$	$\frac{1}{2}$MgOH
34		$Mg(OH)_2 \longrightarrow MgO$[s] $+ H_2O$	$Mg(OH)_2$
35	$MgSiO_3$[s]	$Mg + SiO + 2\,H_2O \longrightarrow MgSiO_3$[s] $+ H_2$	min{Mg, SiO}
36	enstatite	$Mg + SiS + 3\,H_2O \longrightarrow MgSiO_3$[s] $+ H_2S + 2\,H_2$	min{Mg, SiS}
37	(3)	$2\,Mg + 2\,SiH + 6\,H_2O \longrightarrow 2\,MgSiO_3$[s] $+ 7\,H_2$	min{Mg, SiH}
38		$2\,MgOH + 2\,SiO + 2\,H_2O \longrightarrow 2\,MgSiO_3$[s] $+ 3\,H_2$	min{$\frac{1}{2}$MgOH, $\frac{1}{2}$SiO}
39		$2\,MgOH + 2\,SiS + 4\,H_2O \longrightarrow 2\,MgSiO_3$[s] $+ 2\,H_2S + 3\,H_2$	min{$\frac{1}{2}$MgOH, $\frac{1}{2}$SiS}
40		$MgOH + SiH + 2\,H_2O \longrightarrow MgSiO_3$[s] $+ 3\,H_2$	min{$\frac{1}{2}$MgOH, $\frac{1}{2}$SiH}
41		$Mg(OH)_2 + SiO \longrightarrow 2\,MgSiO_3$[s] $+ H_2$	min{$Mg(OH)_2$, SiO}
42		$Mg(OH)_2 + SiS + H_2O \longrightarrow MgSiO_3$[s] $+ H_2S + H_2$	min{$Mg(OH)_2$, SiS}
43		$2\,Mg(OH)_2 + 2\,SiH + 2\,H_2O \longrightarrow 2\,MgSiO_3$[s] $+ 5\,H_2$	min{$Mg(OH)_2$, SiH}
44		$2\,MgH + 2\,SiO + 4\,H_2O \longrightarrow 2\,MgSiO_3$[s] $+ 5\,H_2$	min{MgH, SiO}
45		$2\,MgH + 2\,SiS + 6\,H_2O \longrightarrow 2\,MgSiO_3$[s] $+ 2\,H_2S + 5\,H_2$	min{MgH, SiS}
46		$MgH + SiH + 3\,H_2O \longrightarrow MgSiO_3$[s] $+ 4\,H_2$	min{MgH, SiH}
47	Mg_2SiO_4[s]	$2\,Mg + SiO + 3\,H_2O \longrightarrow Mg_2SiO_4$[s] $+ 3\,H_2$	min{$\frac{1}{2}$Mg, SiO}
48	forsterite	$2\,MgOH + SiO + H_2O \longrightarrow Mg_2SiO_4$[s] $+ 2\,H_2$	min{$\frac{1}{2}$MgOH, SiO}
49	(3)	$2\,Mg(OH)_2 + SiO \longrightarrow Mg_2SiO_4$[s] $+ H_2O + H_2$	min{$\frac{1}{2}$$Mg(OH)_2$, SiO}
50		$2\,MgH + SiO + 3\,H_2O \longrightarrow Mg_2SiO_4$[s] $+ 4\,H_2$	min{$\frac{1}{2}$MgH, SiO}
51		$2\,Mg + SiS + 4\,H_2O \longrightarrow Mg_2SiO_4$[s] $+ H_2S + 3\,H_2$	min{$\frac{1}{2}$Mg, SiS}
52		$2\,MgOH + SiS + 2\,H_2O \longrightarrow Mg_2SiO_4$[s] $+ H_2S + 2\,H_2$	min{$\frac{1}{2}$MgOH, SiS}
53		$2\,Mg(OH)_2 + SiS \longrightarrow Mg_2SiO_4$[s] $+ H_2 + H_2S$	min{$\frac{1}{2}$$Mg(OH)_2$, SiS}
54		$2\,MgH + SiS + 4\,H_2O \longrightarrow Mg_2SiO_4$[s] $+ H_2S + 4\,H_2$	min{$\frac{1}{2}$MgH, SiS}
55		$4\,Mg + 2\,SiH + 8\,H_2O \longrightarrow 2\,Mg_2SiO_4$[s] $+ 9\,H_2$	min{$\frac{1}{2}$Mg, SiH}
56		$4\,MgOH + 2\,SiH + 4\,H_2O \longrightarrow 2\,Mg_2SiO_4$[s] $+ 7\,H_2$	min{$\frac{1}{2}$MgOH, SiH}
57		$4\,Mg(OH)_2 + 2\,SiH \longrightarrow 2\,Mg_2SiO_4$[s] $+ 5\,H_2$	min{$\frac{1}{2}$$Mg(OH)_2$, SiH}
58		$4\,MgH + 2\,SiH + 8\,H_2O \longrightarrow 2\,Mg_2SiO_4$[s] $+ 11\,H_2$	min{$\frac{1}{2}$MgH, SiS}

Notes. The reaction efficiency is limited by the collision rate of the key species, which has the lowest abundance among the reactants. The notation $\frac{1}{2}$ in the r.h.s. column means that only every second collision (and sticking) event initiates one reaction.

References. Data sources for the supersaturation ratios (and saturation vapour pressures): (1) Helling & Woitke (2006), (2) Nuth & Ferguson (2006), (3) Sharp & Huebner (1990), and (4) Woitke et al. (2018).

Table B.1. continued.

Index r	Solid s	Surface reaction	Key species
59	$Al_2O_3[s]$	$2\,Al + 3\,H_2O \longrightarrow Al_2O_3[s] + 3\,H_2$	$^1/_2Al$
60	aluminia	$2\,AlOH + H_2O \longrightarrow Al_2O_3[s] + 2\,H_2$	$^1/_2AlOH$
61	(3)	$2\,AlH + 3\,H_2O \longrightarrow Al_2O_3[s] + 4\,H_2$	$^1/_2AlH$
62		$Al_2O + 2\,H_2O \longrightarrow Al_2O_3[s] + 2\,H_2$	Al_2O
63		$2\,AlO_2H \longrightarrow Al_2O_3[s] + H_2O$	$^1/_2AlO_2H$
64	$CaTiO_3[s]$	$Ca + Ti + 3\,H_2O \longrightarrow CaTiO_3[s] + 3\,H_2$	min{Ca, Ti}
65	perovskite	$Ca + TiO + 2\,H_2O \longrightarrow CaTiO_3[s] + 2\,H_2$	min{Ca, TiO}
66	(3)	$Ca + TiO_2 + H_2O \longrightarrow CaTiO_3[s] + H_2$	min{Ca, TiO_2}
67		$Ca + TiS + 3\,H_2O \longrightarrow CaTiO_3[s] + H_2S + 2\,H_2$	min{Ca, TiS}
68		$CaO + Ti + 2\,H_2O \longrightarrow CaTiO_3[s] + 2\,H_2$	min{CaO, Ti}
69		$CaO + TiO + H_2O \longrightarrow CaTiO_3[s] + H_2$	min{CaO, TiO}
70		$CaO + TiO_2 \longrightarrow CaTiO_3[s]$	min{CaO, TiO_2}
71		$CaO + TiS + 2\,H_2O \longrightarrow CaTiO_3[s] + H_2S + H_2$	min{CaO, TiO}
72		$CaS + Ti + 3\,H_2O \longrightarrow CaTiO_3[s] + H_2S + H_2$	min{CaS, Ti}
73		$CaS + TiO + 2\,H_2O \longrightarrow CaTiO_3[s] + H_2S + 2\,H_2$	min{CaS, TiO}
74		$CaS + TiO_2 + H_2O \longrightarrow CaTiO_3[s] + H_2S$	min{CaS, TiO_2}
75		$CaS + TiS + 3\,H_2O \longrightarrow CaTiO_3[s] + 2\,H_2S + H_2$	min{CaS, TiO}
76		$Ca(OH)_2 + Ti + H_2O \longrightarrow CaTiO_3[s] + 2\,H_2$	min{$Ca(OH)_2$, Ti}
77		$Ca(OH)_2 + TiO \longrightarrow CaTiO_3[s] + H_2$	min{$Ca(OH)_2$, TiO}
78		$Ca(OH)_2 + TiO_2 \longrightarrow CaTiO_3[s] + H_2O$	min{$Ca(OH)_2$, TiO_2}
79		$Ca(OH)_2 + TiS + H_2O \longrightarrow CaTiO_3[s] + H_2S + H_2$	min{$Ca(OH)_2$, TiO}
80		$2\,CaH + 2\,Ti + 6\,H_2O \longrightarrow 2\,CaTiO_3[s] + 7\,H_2$	min{CaH, Ti}
81		$2\,CaH + 2\,TiO + 4\,H_2O \longrightarrow 2\,CaTiO_3[s] + 5\,H_2$	min{CaH, TiO}
82		$2\,CaH + 2\,TiO_2 + 2\,H_2O \longrightarrow 2\,CaTiO_3[s] + 3\,H_2$	min{CaH, TiO_2}
83		$2\,CaH + 2\,TiS + 6\,H_2O \longrightarrow 2\,CaTiO_3[s] + 2\,H_2S + 5\,H_2$	min{CaH, TiS}
84		$2\,CaOH + 2\,Ti + 4\,H_2O \longrightarrow 2\,CaTiO_3[s] + 5\,H_2$	min{CaOH, Ti}
85		$2\,CaOH + 2\,TiO + 2\,H_2O \longrightarrow 2\,CaTiO_3[s] + 3\,H_2$	min{CaOH, TiO}
86		$2\,CaOH + 2\,TiO_2 \longrightarrow 2\,CaTiO_3[s] + H_2$	min{CaOH, TiO_2}
87		$2\,CaOH + 2\,TiS + 4\,H_2O \longrightarrow 2\,CaTiO_3[s] + 2\,H_2S + 3\,H_2$	min{CaOH, TiS}
88	$CaSiO_3[s]$	$Ca + SiO + 2\,H_2O \longrightarrow CaSiO_3[s] + 2\,H_2$	min{Ca, SiO}
89	Wollastonite	$Ca + SiS + 3\,H_2O \longrightarrow CaSiO_3[s] + H_2S + 2\,H_2$	min{Ca, SiS}
90	(4)	$2\,Ca + 2\,SiH + 6\,H_2O \longrightarrow 2\,CaSiO_3[s] + 7\,H_2$	min{Ca, SiH}
91		$CaO + SiO + 1\,H_2O \longrightarrow CaSiO_3[s] + H_2$	min{CaO, SiO}
92		$CaO + SiS + 2\,H_2O \longrightarrow CaSiO_3[s] + H_2S + H_2$	min{CaO, SiS}
93		$2\,CaO + 2\,SiH + 4\,H_2O \longrightarrow 2\,CaSiO_3[s] + 5\,H_2$	min{CaO, SiH}
94		$CaS + SiO + 2\,H_2O \longrightarrow CaSiO_3[s] + H_2S + H_2$	min{CaS, SiO}
95		$CaS + SiS + 3\,H_2O \longrightarrow CaSiO_3[s] + 2\,H_2S + H_2$	min{CaS, SiS}
96		$2\,CaS + 2\,SiH + 6\,H_2O \longrightarrow 2\,CaSiO_3[s] + 2\,H_2S + 5\,H_2$	min{CaS, SiH}
97		$2\,CaOH + 2\,SiO + 2\,H_2O \longrightarrow 2\,CaSiO_3[s] + 5\,H_2$	min{CaOH, SiO}
98		$2\,CaOH + 2\,SiS + 4\,H_2O \longrightarrow 2\,CaSiO_3[s] + 2\,H_2S + 3\,H_2$	min{CaOH, SiS}
99		$CaOH + SiH + 2\,H_2O \longrightarrow CaSiO_3[s] + 3\,H_2$	min{CaOH, SiH}
100		$Ca(OH)_2 + SiO \longrightarrow CaSiO_3[s] + H_2$	min{$Ca(OH)_2$, SiO}
101		$Ca(OH)_2 + SiS + H_2O \longrightarrow CaSiO_3[s] + H_2S + H_2$	min{$Ca(OH)_2$, SiS}
102		$2\,Ca(OH)_2 + 2\,SiH + 2\,H_2O \longrightarrow 2\,CaSiO_3[s] + 5\,H_2$	min{$Ca(OH)_2$, SiH}
103		$2\,CaH + 2\,SiO + 4\,H_2O \longrightarrow 2\,CaSiO_3[s] + 5\,H_2$	min{CaH, SiO}
104		$2\,CaH + 2\,SiS + 6\,H_2O \longrightarrow 2\,CaSiO_3[s] + 2\,H_2S + 5\,H_2$	min{CaH, SiS}
105		$CaH + SiH + 3\,H_2O \longrightarrow CaSiO_3[s] + 4\,H_2$	min{CaH, SiH}
106	$Fe_2SiO_4[s]$	$2\,Fe + SiO + 3\,H_2O \longrightarrow Fe_2SiO_4[s] + 3\,H_2$	min{$^1/_2$Fe, SiO}
107	Fayalite	$2\,Fe + SiS + 4\,H_2O \longrightarrow Fe_2SiO_4[s] + H_2S + 3\,H_2$	min{$^1/_2$Fe, SiS}
108	(4)	$4\,Fe + 2\,SiH + 8\,H_2O \longrightarrow 2\,Fe_2SiO_4[s] + 9\,H_2$	min{$^1/_2$Fe, SiH}
109		$2\,FeO + SiO + H_2O \longrightarrow Fe_2SiO_4[s] + H_2$	min{$^1/_2$FeO, SiO}
110		$2\,FeO + SiS + 2\,H_2O \longrightarrow Fe_2SiO_4[s] + H_2S + H_2$	min{$^1/_2$FeO, SiS}
111		$4\,FeO + 2\,SiH + 4\,H_2O \longrightarrow 2\,Fe_2SiO_4[s] + 5\,H_2$	min{$^1/_2$FeO, SiH}
112		$2\,FeS + SiO + 3\,H_2O \longrightarrow Fe_2SiO_4[s] + 2\,H_2S + H_2$	min{$^1/_2$FeS, SiO}
113		$2\,FeS + SiS + 4\,H_2O \longrightarrow Fe_2SiO_4[s] + 3\,H_2S + H_2$	min{$^1/_2$FeS, SiS}
114		$4\,FeS + 2\,SiH + 8\,H_2O \longrightarrow 2\,Fe_2SiO_4[s] + 4\,H_2S + 5\,H_2$	min{$^1/_2$FeS, SiH}
115		$2\,Fe(OH)_2 + SiO \longrightarrow Fe_2SiO_4[s] + H_2O + H_2$	min{$^1/_2$Fe(OH)$_2$, SiO}
116		$2\,Fe(OH)_2 + SiS \longrightarrow Fe_2SiO_4[s] + H_2S + H_2$	min{$^1/_2$Fe(OH)$_2$, SiS}
117		$4\,Fe(OH)_2 + 2\,SiH \longrightarrow 2\,Fe_2SiO_4[s] + 5\,H_2$	min{$^1/_2$Fe(OH)$_2$, SiH}
118		$2\,FeH + SiO + 3\,H_2O \longrightarrow Fe_2SiO_4[s] + 4\,H_2$	min{$^1/_2$FeH, SiO}
119		$2\,FeH + SiS + 4\,H_2O \longrightarrow Fe_2SiO_4[s] + H_2S + 4\,H_2$	min{$^1/_2$Fe(OH)$_2$, SiS}
120		$4\,FeH + 2\,SiH + 8\,H_2O \longrightarrow 2\,Fe_2SiO_4[s] + 11\,H_2$	min{$^1/_2$Fe(OH)$_2$, SiH}
121	C[s]	$C \longrightarrow C[s]$	C
122	Carbon	$C_2 \longrightarrow 2\,C[s]$	C_2
123	(4)	$C_3 \longrightarrow 3\,C[s]$	C_3
124		$2\,C_2H \longrightarrow 4\,C[s] + H_2$	$^1/_2C_2H$
125		$C_2H_2 \longrightarrow 2\,C[s] + H_2$	C_2H_2
126		$CH_4 \longrightarrow C[s] + 2\,H_2$	$^1/_2CH$